Journal of Materials Science & Technology 232 (2025) 209–226

Contents lists available at ScienceDirect

Journal of Materials Science & Technology

journal homepage: www.elsevier.com/locate/jmst

Research Article

Improving mechanical properties of constrained friction processing Mg-Zn-Ca alloys by modifying texture using multiple pass processing

Ting Chen[a,*], Banglong Fu[a,*], Uceu F.H.R. Suhuddin[a], Tong Shen[a], Gaohui Li[b], Emad Maawad[c], Junjun Shen[a], Jorge F dos Santos[a,d], Jean Pierre Bergmann[e], Benjamin Klusemann[a,f]

[a] Solid State Materials Processing, Institute of Material and Process Design, Helmholtz-Zentrum Hereon, Geesthacht 21502, Germany
[b] Shanghai Key Laboratory of Materials Laser Processing and Modification, Shanghai Jiao Tong University, Shanghai 200240, China
[c] Institute of Materials Physics, Helmholtz-Zentrum Hereon, Geesthacht 21502, Germany
[d] Applied Materials and Manufacturing, Energy and Environment Division, Pacific Northwest National Laboratory, WA 99352, USA
[e] Production Technology Group, Technisiche Universität Ilmenau, Ilmenau 98693, Germany
[f] Institute for Production Technology and Systems, Leuphana University Lüneburg, Lüneburg 21335, Germany

ARTICLE INFO

Article history:
Received 13 November 2024
Revised 1 January 2025
Accepted 14 January 2025
Available online 1 March 2025

Keywords:
Constrained friction processing
Magnesium alloys
Microstructure
Mechanical properties
Texture
Plastic deformation

ABSTRACT

Constrained Friction Processing (CFP), a novel friction-based technique, has been developed to efficiently process fine-grained magnesium (Mg) rods, expanding the potential applications of biodegradable Mg alloys in medical implants. This study investigates the enhancement of mechanical properties through the implementation of multiple pass CFP (MP-CFP) in comparison to the conventional single pass CFP. The results reveal a substantial improvement in compressive yield strength (CYS), ultimate compressive strength, and failure plastic strain by 11 %, 28 %, and 66 %, respectively. A comprehensive analysis of material evolution during processing and the effects of the final microstructure on mechanical properties was conducted. The intricate material flow behavior during the final plunge stage of MP-CFP results in a reduced intensity of local basal texture and macrotexture. The diminished intensity of basal texture, combined with a low geometrical compatibility factor at the top of the rod after MP-CFP, effectively impedes slip transfer across grain boundaries. This leads to a local strain gradient along the compression direction, ultimately contributing to the observed enhancement in mechanical properties. The Mg-0.5Zn-0.3Ca (wt.%) alloy, after texture modification by MP-CFP, exhibits a competitive CYS compared with other traditional methods, highlighting the promising application potential of MP-CFP.

1. Introduction

Magnesium (Mg) alloys have provoked increasing interest in recent years as biodegradable implants owing to their excellent biodegradability, biocompatibility, and osteo-promotive property [1]. The advantageous properties of Mg alloys lie in their closely matched density and elastic modulus with natural bones, resulting in minimal mechanical disparity between the implant and the bone [2]. Additionally, Mg is an essential element in the human body, and its alloys naturally degrade, eliminating the need for subsequent surgery to remove the implant [3]. Presently, Mg alloys find primary applications in the medical field, specifically in tissue engineering scaffolds such as bone repair implants and cardiovascular stents [4].

Nevertheless, Mg and Mg alloys with non-toxic chemical compositions often exhibit inadequate strength and corrosion properties, restricting their suitability as biodegradable implants [5]. A viable solution to address these challenges involves the modification of the underlying microstructure. The modification of microstructure, aiming at achieving refined grains and secondary phases, proves advantages in enhancing mechanical properties, while simultaneously improving biocorrosion resistance [6]. Various thermo-mechanical processing (TMP) methods, such as hot rolling [6–9] and hot extrusion [10–14], along with severe plastic deformation (SPD) techniques like high-pressure torsion (HPT) [15,16], equal-channel angular pressing (ECAP) [17,18] and fric-

---

* Corresponding authors.
E-mail addresses: ting.chen@hereon.de (T. Chen), banglong.fu@hereon.de (B. Fu).

https://doi.org/10.1016/j.jmst.2025.01.026

tion stir processing (FSP) [19,20], have been employed to refine grains and secondary phases through robust thermo-mechanical processing applied on as-cast Mg alloys to improve mechanical strength and corrosion resistance. Gungor and Incesu [8,9] discovered that hot-rolled ZXM300 alloy with finer grains exhibited elevated mechanical properties and a reduced biocorrosion rate (0.029 mm/year), suggesting its potential use as a biodegradable alloy, particularly in fracture bone plate applications. Hofstetter et al. [12,13] determined the mechanical properties of hot-extruded ZX10 and conducted an *in vivo* study, revealing that the hot-extruded ZX10 alloy with micro-grains and nano-size secondary phase particles had excellent mechanical properties, including a yield strength of about 200 MPa, along with slow and uniform *in vivo* degradation without observable hydrogen evolution. Edalati et al. [15] observed that the hardness and tensile strength of pure Mg processed by HPT improved due to grain refinement. Horky et al. [17] applied ECAP to Mg-0.5Zn-0.3Ca (wt.%) (ZX00) alloy, noting that the grain size decreased to 1.5 µm, and the tensile strength increased to >370 MPa after processing, in combination with a low degradation rate. Zhang et al. [20] found that NZ20 alloy processed by FSP exhibited higher elongation and better corrosion resistance in Hank's solution compared to rolled material, credited to grain refinement, a strong basal texture, and a small amount of second phase particles.

Recently, a novel friction-based processing technique, known as constrained friction processing (CFP), has been developed to efficiently produce fine-grained Mg rods [21,22] with improved mechanical properties. The preliminary results have verified the potential applications of CFP for producing biodegradable Mg alloys as medical implants, such as screws and pins for orthopedic and accident surgery applications. For example, by using CFP, the grain size of as-cast ZX00 Mg alloy was decreased from over 1 mm to 3–4 µm in a single process cycle of 3 s, and the compression yield strength (CYS) and ultimate compression strength (UCS) was improved by 350 % and 53 %, respectively [21]. Additionally, it has been reported that CFP is able to break and refine secondary particles, which might contribute to better corrosion resistance [23]. Moreover, in contrast to other TMP and SPD methods, CFP shows significant merits as the elimination of additional preparation steps before operation and external heating, high production efficiency, and substantial savings in labor, cost, and energy, *etc.*, make it a compelling option to produce biodegradable Mg alloys at small scale.

Some TMP and SPD methods, such as hot rolling and ECAP, have demonstrated the ability to further enhance mechanical properties through multiple passes. Li et al. [24] discovered that LAZ532, subjected to 9 passes of hot rolling, exhibited superior strength compared to 3 passes, attributing this improvement to grain refinement and dislocation strengthening. Similarly, Liao et al. [25] reported that the yield strength, ultimate strength, and elongation of Mg-Ag alloys improved with an increasing number of hot rolling passes. Multi-pass hot rolling facilitated the achievement of a homogeneously fine-grained microstructure with a high recrystallization volume, while maintaining a similar (small) grain size. Additionally, Wang et al. [26] noted that multi-pass ECAP not only further refined and uniformized grain size, Mg_2Ca particles, and dynamic precipitates of Mg-Al-Ca-Mn alloys, but also weakened texture, leading to improved mechanical properties.

Inspired by the improved mechanical properties after multi-pass processing as revealed above, in the present study, the multi-pass CFP (MP-CFP) method was proposed and compared to the conventional single-pass CFP (SP-CFP) for ZX00 alloy. The effect of multi-pass on the properties and failure modes was investigated. Additionally, the microstructure and texture were characterized and compared, and the differences in microstructural evolution as well as material flow were revealed through the "stop-action" technique. These findings not only enrich the fundamental theory of CFP, but also present a novel strategy for producing Mg implants with superior mechanical properties.

2. Materials and methods

2.1. Materials

The base material (BM) used in this work was a chill-casting ZX00 alloy ingot [27]. The microstructure of the as-cast ZX00 alloy is shown in Fig. 1(a), revealing the average grain size exceeding 1 mm. The ZX00 ingot was cut into sheets with dimensions of 25 mm (L) × 25 mm (W) × 6 mm (H) for subsequent CFP.

2.2. Experiment procedure

CFP was carried out using the RPS200 process system manufactured by Harms & Wende. The tool system and the CFP procedure are illustrated in Fig. 1(a). The procedure of conventional CFP, *i.e.* SP-CFP, as reported in Ref. [21], can be divided into three stages: 1) Preparation stage, the clamping ring descends, applying a preset force, *F*, to secure the BM against the backing anvil, as shown in Fig. 1(b_1); 2) Plunge stage, the probe, and shoulder start to rotate at a pre-set rotation speed, ω. Simultaneously, the shoulder plunges into the BM while the probe ascends, ensuring the volume of the material remains balanced, as shown in Fig. 1(b_2); 3) Final stage, when the shoulder arrives at the maximum plunge depth, *D*, after pre-set plunging time, *t*, the tool system stops rotating and retracts, and a processed rod with the same diameter of the probe is produced, as shown in Fig. 1(b_3).

This work introduced a novel MP-CFP, as depicted in Fig. 1. Compared to SP-CFP, one or more process cycles consisting of plunge stages, retraction stages, and initiation stages are added into the procedure, as shown in Fig. 1(c_1–c_3). In the retraction stage and initiation stage, the shoulder and probe rotate and return to the initial position. An extra couple of plunge and retraction stages are defined as an extra pass of CFP. After every pass, the material is cooled with compressive air to room temperature within a short time. According to our preliminary work, an optimized processing parameter was adapted to obtain defect-free rods with fine grains. The clamping force, rotation speed of the tool, plunge depth, and plunge time were set as 12 kN, 1800 rpm, 3 mm, and 3 s, respectively. SP-CFP, double pass CFP (2 × MP-CFP) and triple pass CFP (3 × MP-CFP) were investigated. The diameter of the probe, shoulder, and clamping ring are 6 mm, 9 mm, and 17 mm, respectively. As a result, the height of the obtained rod was 6.75 mm, and the diameter was 6 mm. The experimental reference frame of CFP is defined by the radial longitudinal direction (RLD), radial transverse direction (RTD), and extrusion direction (ED) as shown in Fig. 1.

Moreover, in order to understand the material flow and deformation behaviors in SP-CFP and MP-CFP, tracer experiments were conducted. Carbon nanotubes (CNTs), used as material tracers, were inserted into a hole with a diameter of 0.7 mm and a depth of 4 mm, situated 1.5 mm away from the rotation axis at the upper surface before the final plunge stage of CFP. Subsequent to the CFP procedure, the distribution of CNTs in the longitudinal section, *i.e.*, ED-RTD section, of the rod was further characterized to investigate the materials flow behavior by comparisons drawn against the initial placement of CNTs.

2.3. Microstructure characterization

After CFP, the longitudinal cross-section of the produced rod was machined, ground, and polished according to standard preparation of metallographic samples. The colored overview optical

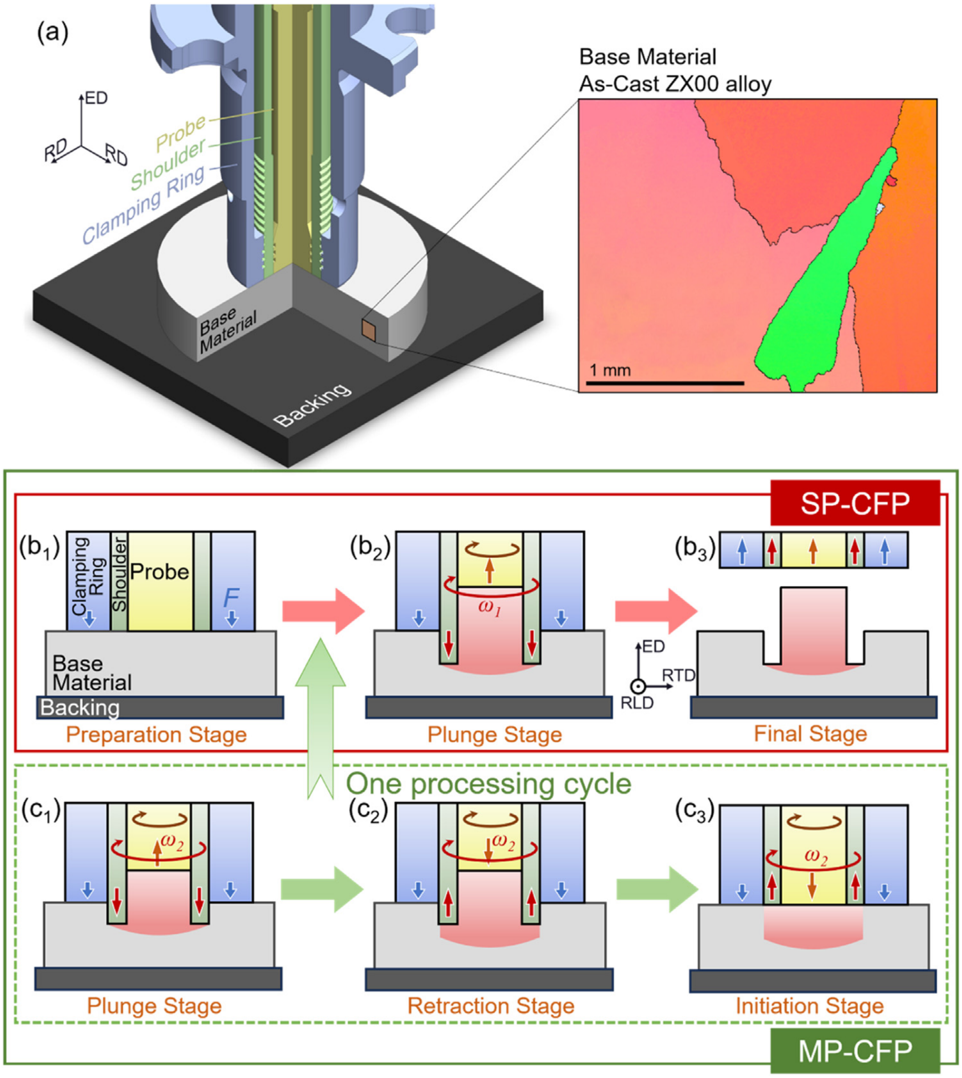

Fig. 1. Schematic drawings of the procedure of CFP: (a) tool system and microstructure of as-cast ZX00 alloy, (b_1, b_2, b_3) conventional SP-CFP, (c_1, c_2, c_3) the process cycle added in MP-CFP.

metallograph (OM) was obtained by a LEICA DMi8 OM equipped with polarized light plus sensitive tint after the polished sample was etched by acetic-picral etchant. The electron backscattered diffraction (EBSD) measurement was performed by an FEI Quanta 650 field emission gun scanning electron microscope (SEM) equipped with an EDAX Velocity EBSD detector after the samples were electricity polished by AC2 solution with the voltage of 25 V at −20 °C for 35 s. The data from EBSD was analyzed by both TSL OIM 8 and MTEX 5.10. The critical threshold between low angle grain boundary (LAGB) and high angle grain boundary (HAGB) was 15°. The recrystallized grains were distinguished according to grain orientation spread (GOS) from EBSD. The grains characterized by a GOS lower than 2° were defined as recrystallized grains [28]. The scanning transmission electron microscopy (STEM) was carried out by Thermo Fisher Helios 5 PFIB. Additionally, the global macrotexture measurement was carried out at the P07 beamline which is partly operated by the Helmholtz-Zentrum Hereon at PETRA III of the German Electron Synchrotron (DESY) in Hamburg. Different vertical positions of the CFP rod, 1 mm, 3 mm, and 5 mm from the top of the rod, were examined in transmission mode by a monochromatic X-ray beam with the energy of 87.1 keV and size of 0.5×0.5 mm^2, see supplementary Fig. S1 in supplementary material. The pole figures (PFs) were obtained using Fit2D [29] and the in-house code package SABO developed by Yi et al. [30].

2.4. Compression test

In general, Mg implants, such as intramedullary nails, dental implant body, and abutment, primarily undergo compressive loadings. Therefore, the current investigation focuses on evaluating the compression properties. The specimens were machined into cylindrical samples with a height of 6 mm and a diameter of 6 mm for compression tests. The compression tests were conducted at room temperature by a Zwick/Roell 1478 universal testing machine at a strain rate of 10^{-3} s^{-1}. Three repetitions of each condition were conducted. Digital image correlation (DIC) was used to analyze the local deformation behavior in 4 mm × 4 mm at the center of the CFPed samples during the compression test, in which images were captured at a fixed rate of 5 Hz by the GOM ARAMIS system. After the compression test, the fractured compression samples were scanned by a Yxlon Y Cougar X-ray inspection system and reconstructed by ImageJ to reveal the three-dimensional (3D) characteristics of the fractured cracks.

To further understand the compression deformation mechanism, an in-plane compression sample with a width of 5.8 mm (RD), a height of 6 mm (ED), and a thickness of 1 mm (RD) was cut from the center of the processed rod for in-plane compression test, which can provide a flat surface for EBSD characterization. The in-plane compression test was conducted at room temperature us-

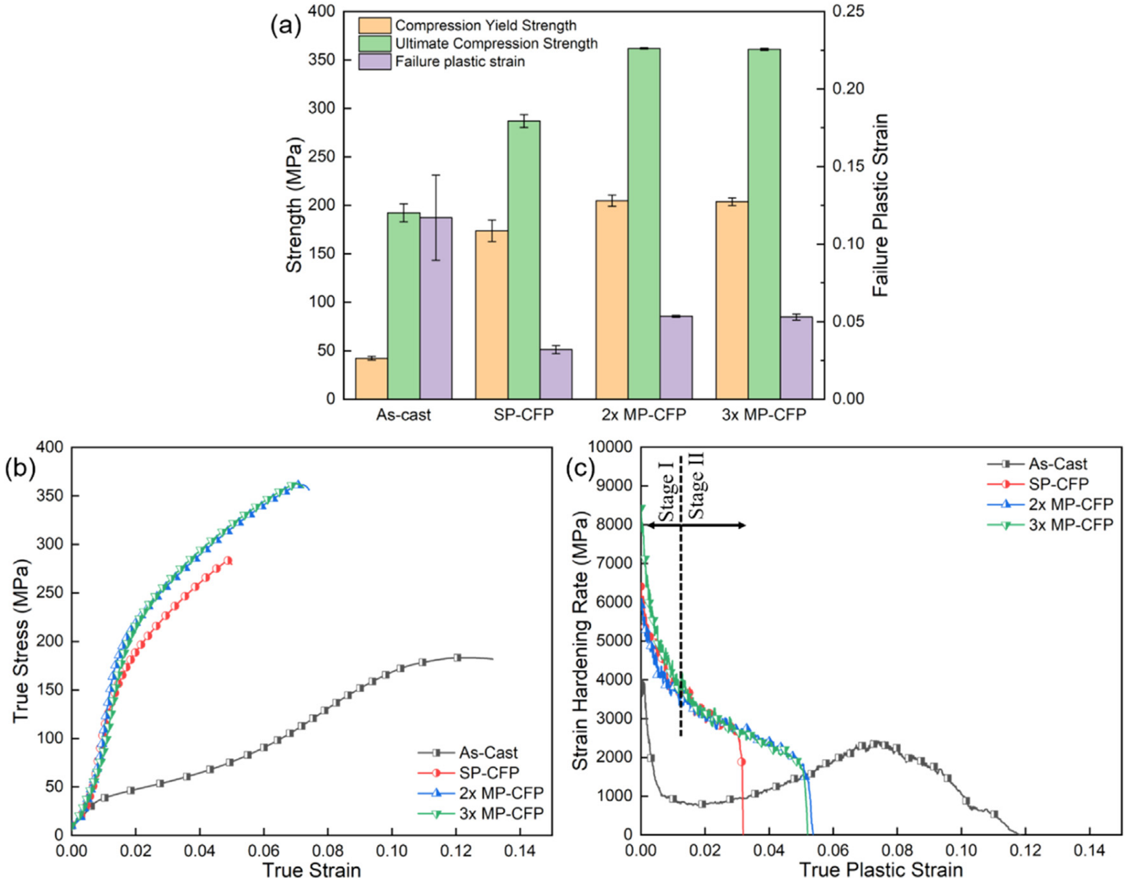

Fig. 2. Compression behavior of rods obtained by as-cast, SP-CFP, 2 × MP-CFP, and 3 × MP-CFP. (a) Compression properties, (b) stress-strain curve, (c) strain hardening rate curve. The true plastic strain is defined as the true strain after the stress exceeds yield strength.

ing DEBEN in-situ compression stage with a 5 kN load cell at a speed of 0.006 mm/s, which is equal to the strain rate conducted in the previous compression test by the universal testing machine. The initial microstructure of the sample in the RD-ED plane prior to the compression test and after the compression test at a strain of 3 % was characterized by OM and SEM with EBSD.

3. Result

3.1. Compression properties

The compression properties of as-cast, SP-CFP, 2 × MP-CFP, and 3 × MP-CFP samples are illustrated in Fig. 2. SP-CFP has already significantly enhanced both CYS and UCS of the as-cast ZX00 alloy, with an even more pronounced improvement observed for MP-CFP. In comparison to SP-CFP, 2 × MP-CFP significantly improves the CYS of ZX00 alloy from 175 MPa to 205 MPa, by 17 %, UCS from 287 MPa to 362 MPa, by 26 %, and failure plastic strain by a remarkable 66 % increase, as shown in Fig. 2(a). The work hardening rate curves are calculated based on the compression results, as shown in Fig. 2(c), to further understand the compression behavior of CFP alloys. The strain hardening rate curves exhibits notable distinctions between as-cast and CFP alloys. In the as-cast alloy, the strain hardening rate exhibits a distinct ascending stage after the initial sharp decreasing stage due to the larger grain size, enhancing the storage rate of dislocation and activation of tension twinning. In contrast, the initial strain hardening rate of the CFPed sample is significantly higher due to the grain refinement. The strain hardening rate decreases sharply during Stage I due to elastoplastic transition, followed by a linear decrease during Stage II. 2 × MP-CFP alloy exhibits a wider Stage II, contributing to a higher plasticity and failure strain compared to SP-CFP. However, when the number of process cycles is further increased, *i.e.* from 2 × MP-CFP to 3 × MP-SCP, the compression properties are quite similar.

A one-way ANOVA followed by Tukey post-hoc tests using Minitab software was performed to evaluate the statistical significance of the observed improvements, as shown in supplementary Tables S1–S3. The results of the statistical analysis confirm that the improvement of MP-CFP is significant. However, the differences in mechanical properties between 2 × MP-CFP and 3 × MP-CFP were found to be not statistically significant, indicating that the differences in compression properties between SP-CFP and MP-CFP resulted from the first process cycle. Consequently, to reveal the potential mechanisms, only 2 × MP-CFP was further investigated in detail in the current study, denoted simply as MP-CFP in the following.

In order to delve into the compression mechanism and understand the rationale behind the improved mechanical properties for MP-CFP, the strain field during the compression test was determined by DIC, as depicted in Fig. 3. For the as-cast Mg alloy, the local strain is notably concentrated along a plane at an angle of approximately 45° to the horizontal plane. As the compression test progresses, the strain concentration along the identified plane increases, culminating into the fracture. The strain field of the CFPed sample is homogeneous horizontally during the compression test, but it is higher at the top compared to the bottom of the rod. Ultimately, with SP-CFP, local strain at the bottom of the rod increases significantly, leading to failure. In contrast, with MP-CFP, local strain increases at the middle of the rod, resulting in fracture along a curved plane located in the middle of the rod.

Fig. 3(b) presents the local strain profile along the center line in compression direction at different global strains. When com-

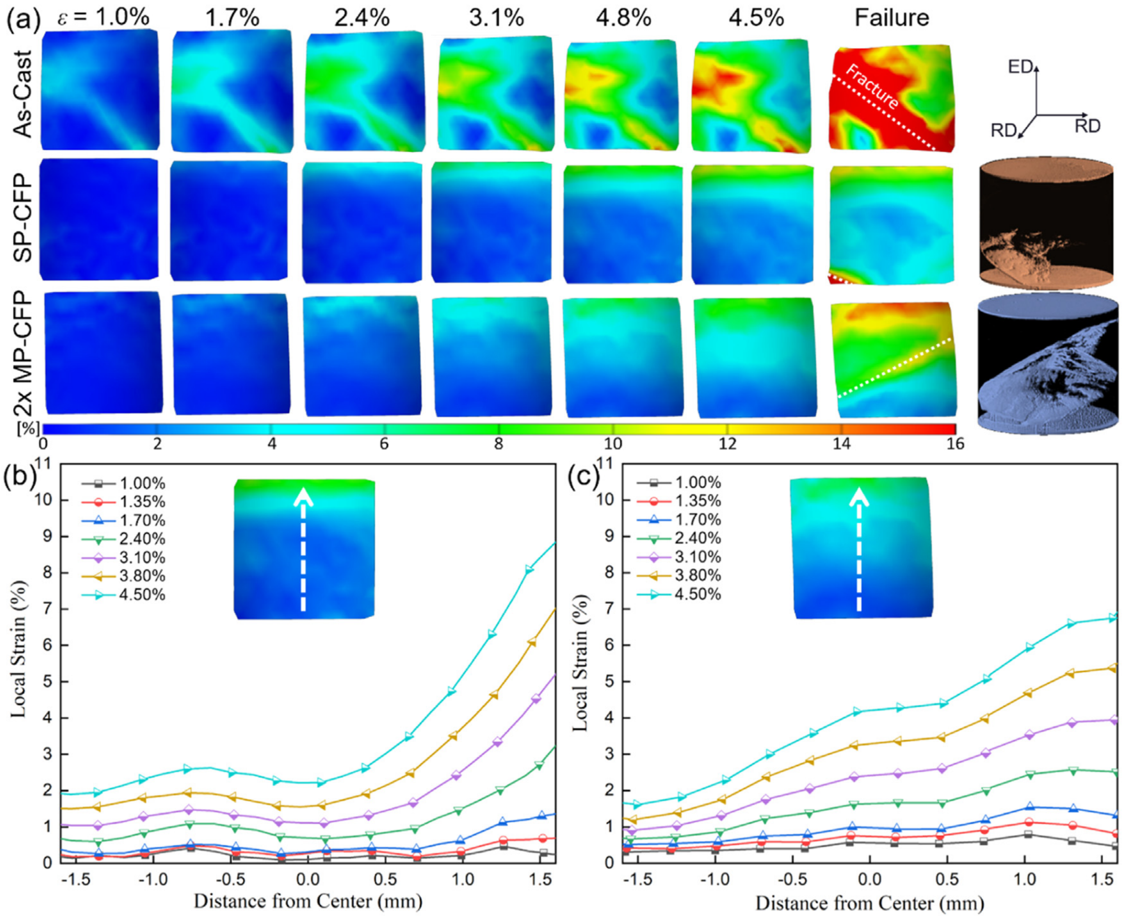

Fig. 3. (a) Captured image series of equivalent strain field evolution of as-cast, SP-CFP, and MP-CFP samples during compression test and 3D fracture reconstruction after failure. Strain profile along gauge pattern in compression direction at different global strains for (b) SP-CFP and (c) MP-CFP samples.

pression stress exceeds the yield point, strain distribution is non-uniform along the compression direction after CFP. Local strain at the top consistently surpasses that at the bottom. Global compression strain of SP-CFP is primarily contributed by the local strain concentration at the top, while the center and bottom exhibit similarly lower values. In MP-CFP, the local strain concentration is alleviated and the strain field displays a gradient along the compression direction. This gradient in terms of the local strain distribution may be a key factor contributing to the observed improvement in strength and failure plastic strain.

3.2. Microstructure

3.2.1. Microstructure after the first process cycle

To investigate the effects of the first process cycle, the microstructure after one process cycle was characterized by OM and EBSD, as shown in Fig. 4. The PFs and inverse pole figure (IPF) map, as marked in the macrograph in Fig. 4(a), are presented in Fig. 4(b, c), respectively. In comparison to the as-cast material, average grain size (GS) decreases significantly after first pass processing, diminishing from over 1 mm to about 5–6 μm. The first process cycle of MP-CFP induced a strong basal texture with high intensity of texture, $I_{\max}$, ranging from 40 to 90 multiples of a random distribution (m.r.d). The [0002] direction at the rotation axis is parallel to ED. Moving from the rotation axis to the edge of the processing region, *i.e.*, shoulder plunging region, the angle between [0002] direction and ED increases to about 40°, depicting a concave basal plane, which aligns well with findings reported in Mg alloys after refill friction stir spot welding by Fu et al. [31]. Compared to the original as-cast material with large grain size and random texture, the microstructure after the first pass processing was characterized by refined grain size and strong basal texture, exerting significant influence on material flow behavior and the ultimate microstructure after MP-CFP.

3.2.2. Microstructure after MP-CFP

The microstructure of the rod produced by MP-CFP is shown in Fig. 5, with specific regions marked in Fig. 5(a) for analysis by EBSD. The grain morphologies represented by IPF maps correspond to the marked position in Fig. 5(b). In comparison to the material after first pass processing, as shown in Fig. 4(c), the average GS slightly decreases to approximately 3–6 μm after MP-CFP. The grain size at the top and bottom is slightly smaller, around 3–4 μm, while the grain size at the center is slightly larger, approximately 5–6 μm. There is no noticeable deviation in grain size along the RTD.

Further analysis of the local textures in the marked subregions was conducted, and the [0002] PFs are presented in Fig. 5(c). CFP generates a strong basal texture with a local $I_{\max}$ of the basal pole ranging from 11 to 97 m.r.d. Along the rotation axis, the [0002] basal pole peak is nearly parallel to the ED, and albeit divided into two peaks at the middle of the rod with the local $I_{\max}$ about 20–40 m.r.d. The local $I_{\max}$ is much lower at the top, about 10 m.r.d, while it was much higher at the bottom, >80 m.r.d. As the distance from the rotation axis increases, the angle between the [0002] di-

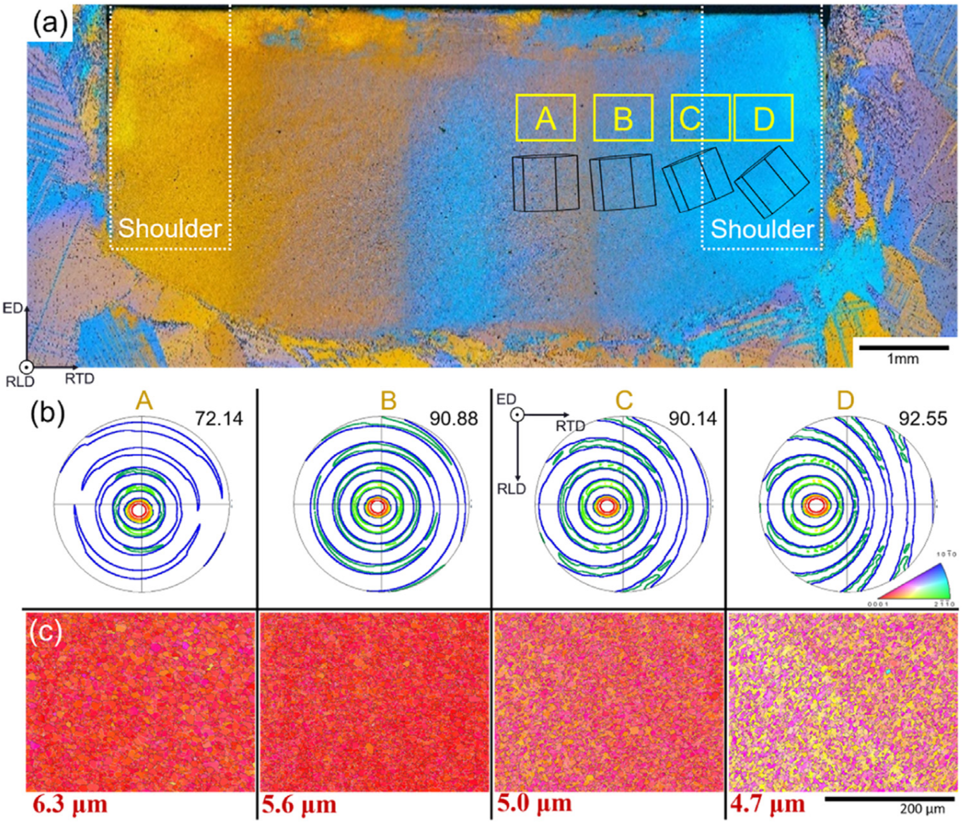

Fig. 4. (a) Microstructure of ZX00 alloy after first pass processing, including (b) [0002] PFs with intensity, $I_{\max}$, and (c) IPF maps colored orientation maps with average grain size corresponding to the position marked by yellow rectangles in (a).

rection and ED increases, revealing a gradient orientation of the basal plane and a convex dome shape globally.

The typical microstructure characteristics, such as GS and intensity of texture, $I_{\max}$, along the rotation axis obtained by SP-CFP and MP-CFP are further compared in Fig. 6 to investigate factors affecting the improvement of mechanical properties when MP-CFP was adopted. Compared to SP-CFP, the grain size at the top of the processed rod obtained by MP-CFP is slightly lower, while that at the middle and bottom is a bit larger. Additionally, the previous work on CFP conducted by the authors has reported that the effect of grain size in CFP samples on mechanical properties is low due to the strong basal texture [21]. Therefore, the substantial improvement in mechanical properties with MP-CFP is attributed to other factors, such as texture. The $I_{\max}$ of the basal pole along the rotation axis in SP-CFP is more homogeneous compared to MP-CFP. Furthermore, $I_{\max}$ at the top obtained with SP-CFP is much higher than that with MP-CFP, whereas it is much lower at the bottom, indicating that the top of the rod might exhibit better local strength due to the weaker texture [32], resulting in lower local strain at the top compared with SP-CFP. Additionally, the orientation distribution function (ODF) at the middle part of SP-CFP and MP-CFP samples, marked in Fig. 6(a), was calculated to further compare the difference of texture, as shown in Fig. 6(b, c). Both microstructures of SP-CFP and MP-CFP samples exhibit a strong basal fiber texture, with a direction near [0002]//ED. There is no distinct basal pole peak separation in SP-CFP, while clear double peaks are observed in MP-CFP, which are beneficial for the ductility of Mg alloys [33]. The weaker texture at the top and the disparity in texture in the middle of the processed rod between SP-CFP and MP-CFP may be the primary reason for the observed differences in mechanical properties.

Macrotexture analysis is necessary since the macrotexture in Mg alloys plays an important role in global mechanical properties [31]. Macrotexture analysis using synchrotron radiation aimed to further compare the distribution of macrotexture along the ED direction between SP-CFP and MP-CFP, offering insights into the enhanced mechanical properties observed with MP-CFP. Macro PFs with $I_{\max}$ at different heights were calculated, as illustrated in Fig. 7. The direction of basal pole peaks of macrotexture exhibits similarity in rods obtained by SP-CFP and MP-CFP, maintaining an alignment of [0002]//ED. For SP-CFP, $I_{\max}$ of [0002] macrotexture at different heights remained similar, ranging from 45 to 55 m.r.d. However, after MP-CFP, $I_{\max}$ at the top and middle significantly decreases to 15 and 34 m.r.d., respectively, attributed to irregular material flow behavior in these regions. One of the diffraction patterns at the top with SP-CFP and MP-CFP are depicted in Fig. 7(c, d), respectively. The [0002] rings in diffraction patterns with SP-CFP and MP-CFP exhibit higher intensity in the ED direction. The diffraction pattern is more dispersed with MP-CFP, presenting more isotropic and complete diffraction rings, which indicates a weaker macrotexture. Additionally, STEM analysis was performed on MP-CFPed ZX00 alloys to investigate the precipitates, as shown in Fig. S2. Only a small number of precipitates with low volume fractions are observed. Therefore, the improvement in mechanical properties achieved with MP-CFP compared to SP-CFP may primarily stem from texture weakening.

3.3. Material flow behavior

Material flow behavior during CFP is closely related to texture evolution. To explore the correlation between texture and material flow behavior during the plunge stage (final plunge stage in case of

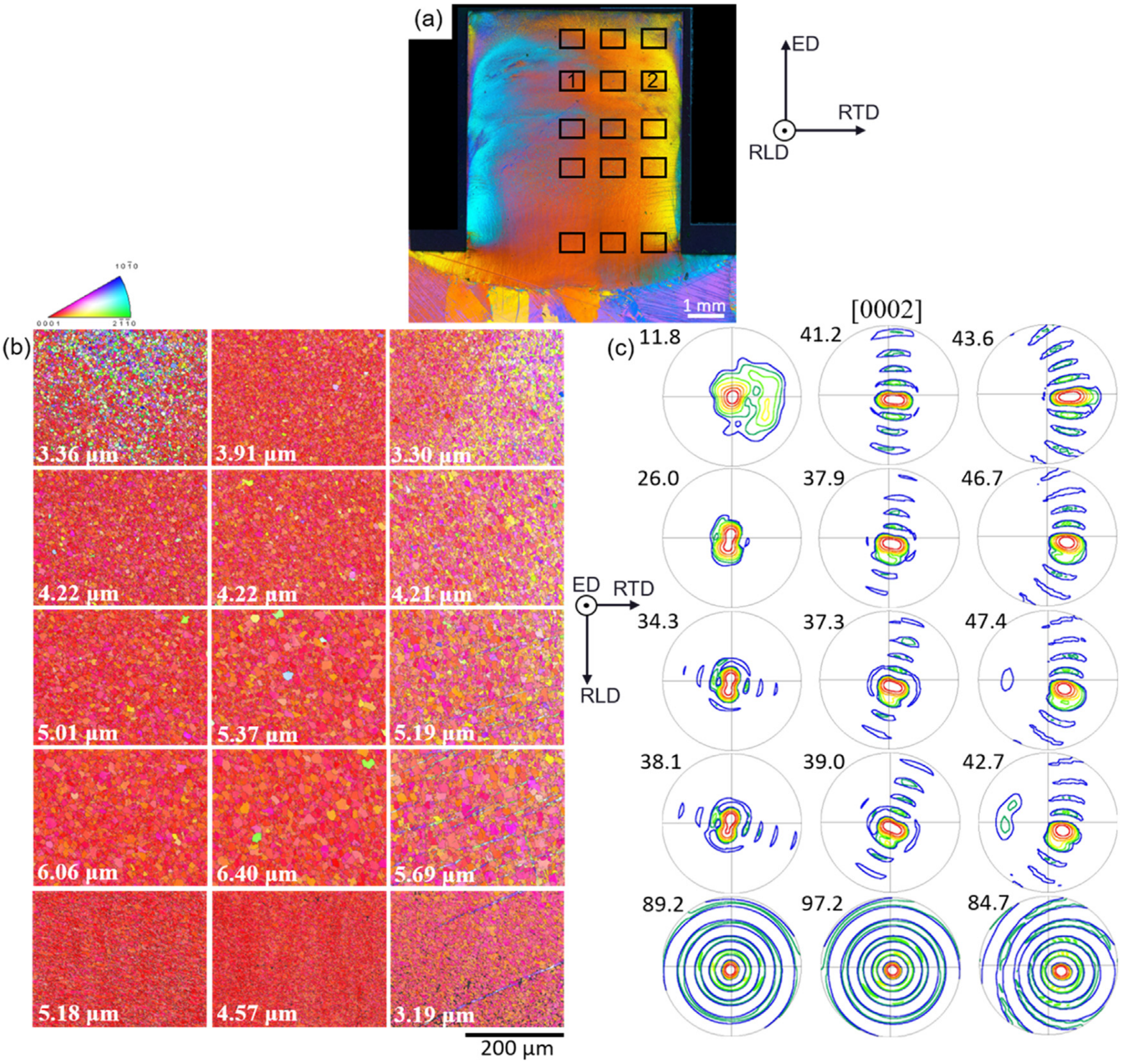

Fig. 5. (a) Microstructure of ZX00 alloy obtained by MP-CFP, including (b) IPF maps colored orientation maps with average grain size and (c) [0002] PFs with intensity, I_{max}, corresponding to the position marked by black rectangles in (a).

MP-CFP), tracer experiments employing SP-CFP and MP-CFP were conducted, where the resulting longitudinal sections after CFP are depicted in Fig. 8(a, b). In the tracer experiments, the severe shear strain induced by the rotated tool during CFP causes the distribution of CNTs to transition from a straight wire to a spiral shape with a low helix angle. CNTs layers in the rod subjected to SP-CFP exhibit regularity throughout the entire rod, whereas those in the rod undergoing MP-CFP appear disordered, particularly in the middle and at the top of the rod. These irregular CNTs layers indicate the complex materials flow behavior during the final plunge stage of MP-CFP. The materials flow behavior is closely related to the microstructure with fine grains and strong basal texture after the first pass processing. Furthermore, a substantial area on the cross-section at the midpoint of the rod was characterized by EBSD. Euler maps of the detected regions were analyzed, as shown in Fig. 8(c, d), highlighting the disparity in grain orientation across different areas. In the case of SP-CFP, owing to the uniform material flow behavior, the grains in the cross-sectional plane exhibit a regular gradient orientation distribution. Conversely, material flow behavior during MP-CFP proves irregular, resulting in disorderly grain orientations near the rotation axis, presenting a weaker local basal texture and multiple basal pole peaks, as depicted in Fig. 6(c).

4. Discussion

4.1. Material flow and microstructure evolution in CFP

The results regarding the macro- and microstructure observations of SP-CFP and MP-CFP have revealed that, compared to SP-CFP, MP-CFP rod shows irregular material flow behavior and weakened macrotexture with pole peak separation at the center. The material flow behavior and microstructure evolution were further analyzed and discussed to understand the underlying mechanisms resulting in the material evolution differences between SP-CFP and MP-CFP.

4.1.1. Material flow behaviors

As shown above, the material flow behavior was more irregular when MP-CFP was adopted. To further understand the reason for the difference in materials flow behavior between SP-CFP and MP-CFP, the “stop action” technique [34], an effective method beneficial to understanding material evolution during processing, was employed when the plunge depth 0.7 mm and 2 mm were reached. The microstructure of the longitudinal section is shown in Fig. 9. Tracer experiments combined with the “stop action” technique for a plunge depth of 2 mm were addition-

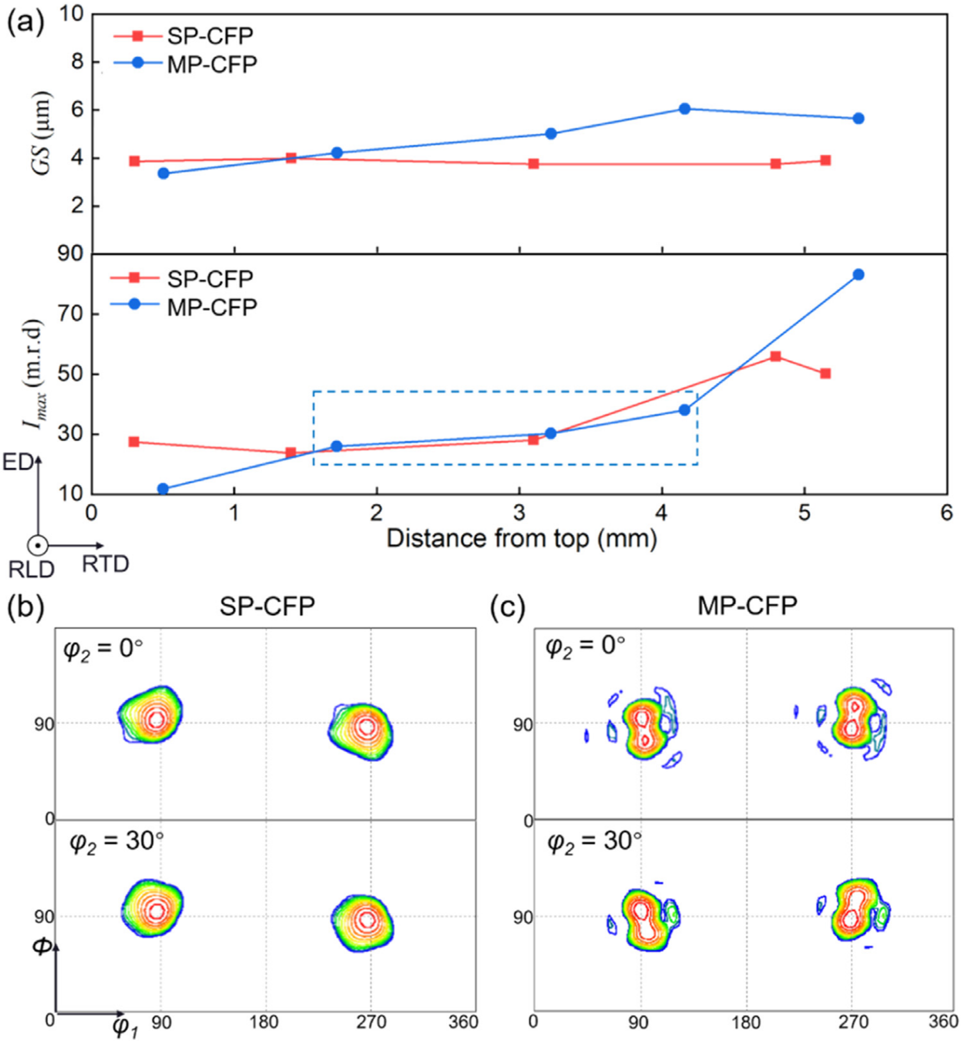

Fig. 6. Comparison of microstructure characteristics along rotation axis obtained by SP-CFP and MP-CFP. (a) GS and intensity of texture, I_{max}. ODF at the middle part, marked in the blue rectangle in (a), with (b) SP-CFP and (c) MP-CFP.

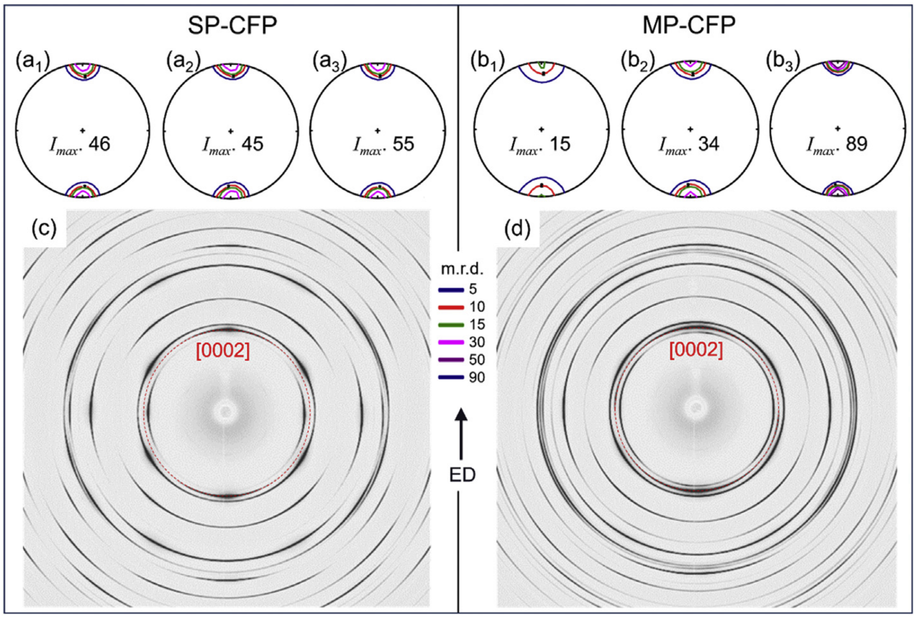

Fig. 7. (0002) PFs showing macrotexture with I_{max} of the (a_1, b_1) top, (a_2, b_2) middle, and (a_3, c_3) bottom sections of rod produced by (a) SP-CFP and (b) MP-CFP, respectively. The diffraction patterns at the top of the rod are produced by (c) SP-CFP and (d) MP-CFP.

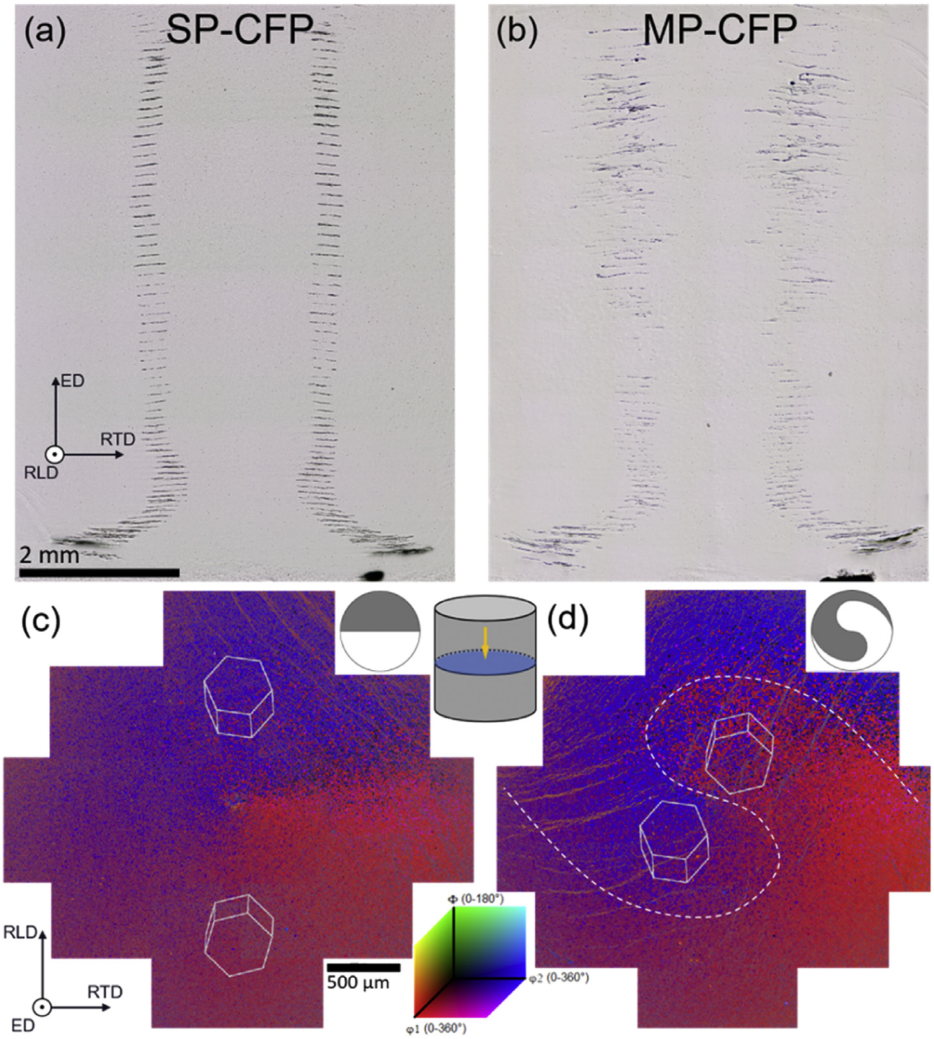

Fig. 8. CNTs distribution after tracer experiments with (a) SP-CFP and (b) MP-CFP. Euler maps of the cross-section at the middle of the rod produced by (c) SP-CFP and (d) MP-CFP colored by grain orientation.

ally conducted. The distribution of CNTs in the longitudinal section of the rod was further characterized after CFP, as shown in Fig. 9(a_3, b_3). Additionally, the temperature history during SP-CFP and the final pass of MP-CFP were measured, as shown in Fig. S3. Their temperature histories are similar, with a peak temperature of about 400 °C.

For SP-CFP, at the early stage, the temperature was low, making material deformation challenging, resulting in a narrow Stir Zone (SZ) region. For instance, the microstructure at the root of the rod retained the original large grains, as shown in Fig. 9(a_1). As the shoulder plunged, the accumulated heat produced from friction increased the material temperature, enhancing plasticity and increasing the proportion of SZ area, as shown in Fig. 9(a_2). It is well accepted that the critical resolved shear stress (CRSS) of basal slip in Mg is lower than that of the other slip system at low temperature [35,36]. For the final plunge stage in MP-CFP, microstructure after prior processing pass exhibited a stronger basal texture, with the direction of the basal plane being similar to the shear plane during the final plunge stage, resulting in plastic deformation under lower shear stress. Additionally, the refined grains after the prior processing pass provided higher grain boundary density, resulting in a reduction of deformation resistance at high temperature due to activation of grain boundary sliding. Therefore, material after the prior processing pass is more prone to plastic deformation during the final plunge stage in MP-CFP, resulting in a larger volume of SZ, as shown in Fig. 9(b_1, b_2).

In the tracer experiments, the distribution of CNTs was more regular in the rod using SP-CFP, whereas it appeared disorderly at the top of the rod using MP-CFP, as shown in Fig. 9(a_3, b_3). The shear strain (γ) can be estimated by the distance (d) between spiral CNTs layers [21], as shown in Fig. S4, which is proportional to d. The distance between the CNTs layer with the edge of SZ in MP-CFP (d_2 = 0.76 mm) is nearly twice as large as in the SP-CFP (d_1 = 0.39 mm), indicating a lower gradient of rotation displacement and shear strain rate ahead of the SZ during the final plunge stage of CFP. This observation corresponds to the results shown in Fig. 8 and further supports the notion that the material is more prone to deform and flow during the final plunge stage of MP-CFP, resulting in a lower shear strain rate and less material stirring. It has been reported that the shear texture strength decreases as the strain rate reduces [37,38]. Additionally, less material stirring leads to disparities in grain orientation across different areas, as shown in Fig. 8(d). This contributes to both weaker local textures, as shown in Figs. 5 and 6, and a reduction in macrotexture intensity, as shown in Fig. 7, at the upper part of the MP-CFPed rod. As the SZ during the final plunge stage expands into the previous SZ, the presence of large grains with random orientations beneath the SZ enhances the shear strain rate. This results in a higher texture

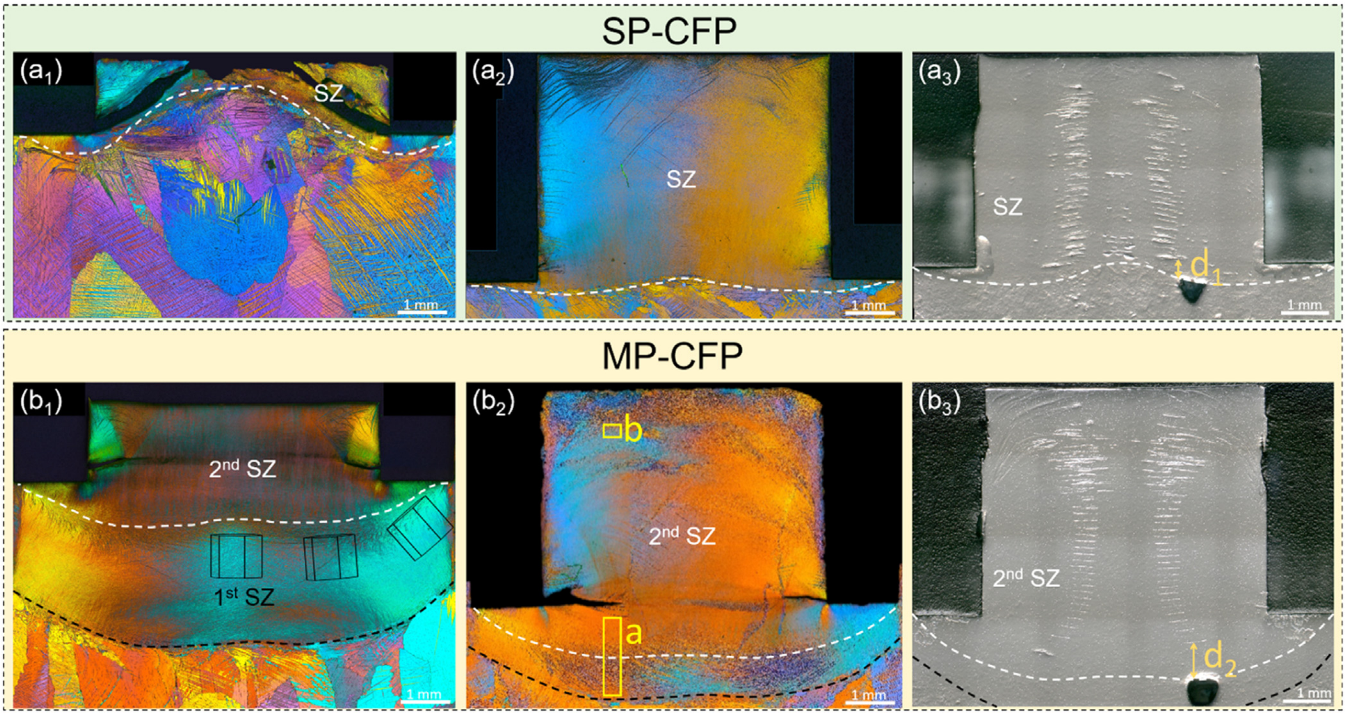

Fig. 9. Microstructures obtained by "stop action" experiments during (a) SP-CFP and (b) the final plunge stage of MP-CFP with plunge depth of (a_1, b_1) 0.7 mm and (a_2, b_2) 2 mm. (a_3, b_3) Microstructure obtained by tracer experiments using CNTs combined with "stop action" technique for a plunge depth of 2 mm.

intensity at the bottom of the MP-CFPed rod, as shown in Figs. 5 and 6.

4.1.2. Microstructure evolution

To comprehend the microstructure evolution during the final plunge stage of MP-CFP and further investigate the reason for the different final texture between SP-CFP and MP-CFP, the regions at the SZ in the rod and transition zone between SZ and thermo-mechanically affected zone (TMAZ) at the final plunge stage of MP-CFP, *i.e.*, region a and b inside marked in Fig. 9(b_2), were examined using EBSD, as illustrated in Fig. 10. The IPFs colored by grain orientation and GOS maps of different subregions marked in Figs. 9(b_2) and 10(a) are presented in Fig. 10(b_1–f_1) and (b_2–f_2), respectively. The misorientation and grain size distribution were further analyzed, as shown in Fig. 10(b_3–f_3) and (b_4–f_4).

The four main proposed recrystallization mechanisms in Mg alloys are grain boundary nucleation (GBN) [28,39], deformation twin nucleation (DTN) [40,41], shear band nucleation (SBN) [42,43], and particle-stimulated nucleation (PSN) [44,45]. The recrystallization mechanism during SP-CFP of Mg alloys has been reported by authors [21] as follows: Since the grain size of the original as-cast material is large, twinning is easier to activate than non-basal slip at low temperature. Thus, DTN is the main recrystallization mechanism at the early stage. As the temperature increases, PSN plays a main role since there are some secondary phase particles in the as-cast material, providing nucleation positions for recrystallization. As the grains become finer, the main recrystallization transforms to GBN due to the increase of grain boundaries and dissolution of secondary particles.

In the case of MP-CFP, the fine-grained microstructure produced by the prior processing pass inhibits twinning [46,47], and PSN is not observed due to the total solid dissolution of secondary particles, as shown in Fig. S5. There is no obvious difference in grain size between SZ after the prior processing pass and TMAZ during the final plunge stage of MP-CFP, as shown in Fig. 10(f_4). Recrystallization has not started due to the low temperature and deformation, and the average GOS increases, as shown in Fig. 10(f_2). Compared with SP-CFP, the gradient of GS and GOS at TMAZ decreases during the final plunge stage of MP-CFP due to the lower gradient of shear strain. The main recrystallization mechanism at the early stage at low temperature in region e in Fig. 10, near the interface between SZ and TMAZ, is SBN with activation of basal slip, attributed to the refined grains and strong basal texture. The average grain size decreases, and the fraction of recrystallized grains, *i.e.* GOS $< 2°$ [28], increases, as shown in Fig. 10(e_3, e_4). It is generally accepted that the orientation of recrystallized grains produced by SBN is usually random [42,48]. Compared with the SZ after first pass processing, as shown in region B–D in Fig. 4, and the TMAZ during the final plunge stage of MP-CFP, as shown in region f in Fig. 10, there are several shear bands present, including fine recrystallized grains with much different grain orientation compared to the original microstructure in region e. The proportion of misorientation higher than 35° increases. As the shoulder plunges down, shear bands disappear gradually with a decrease in the proportion of misorientation higher than 35°, from 19.2 % to 4.8 %, and the grain size further decreases, as shown in Fig. 10(c, d). In this stage, the main recrystallization mechanism transitions from SBN to GBN due to the decrease in grain size and the increase in temperature. The basal plane of recrystallized grains from SBN is rotated to be parallel to the shear plane, leading to a strong B-fiber basal texture. At the same time, the material starts to experience severe shear deformation and flow. When the material is extruded into the rod, as shown in Fig. 10(b), the shear strain rate decreases, resulting in an increase in the fraction of recrystallized grains and average grain size. Additionally, the fraction of low angle misorientation (2°–10°) decreases, while the fraction of moderate angle misorientation (15°–35°) increases, indicating a gradual LAB-to-HAB transformation, *i.e.*, continuous dynamic recrystallization in the rod [49].

The schematic material flow behavior and microstructure evolution during the SP-CFP and MP-CFP is illustrated in Fig. 11. The gradient of rotation displacement and shear strain ahead of the SZ during MP-CFP is lower due to refined grains as well as strong

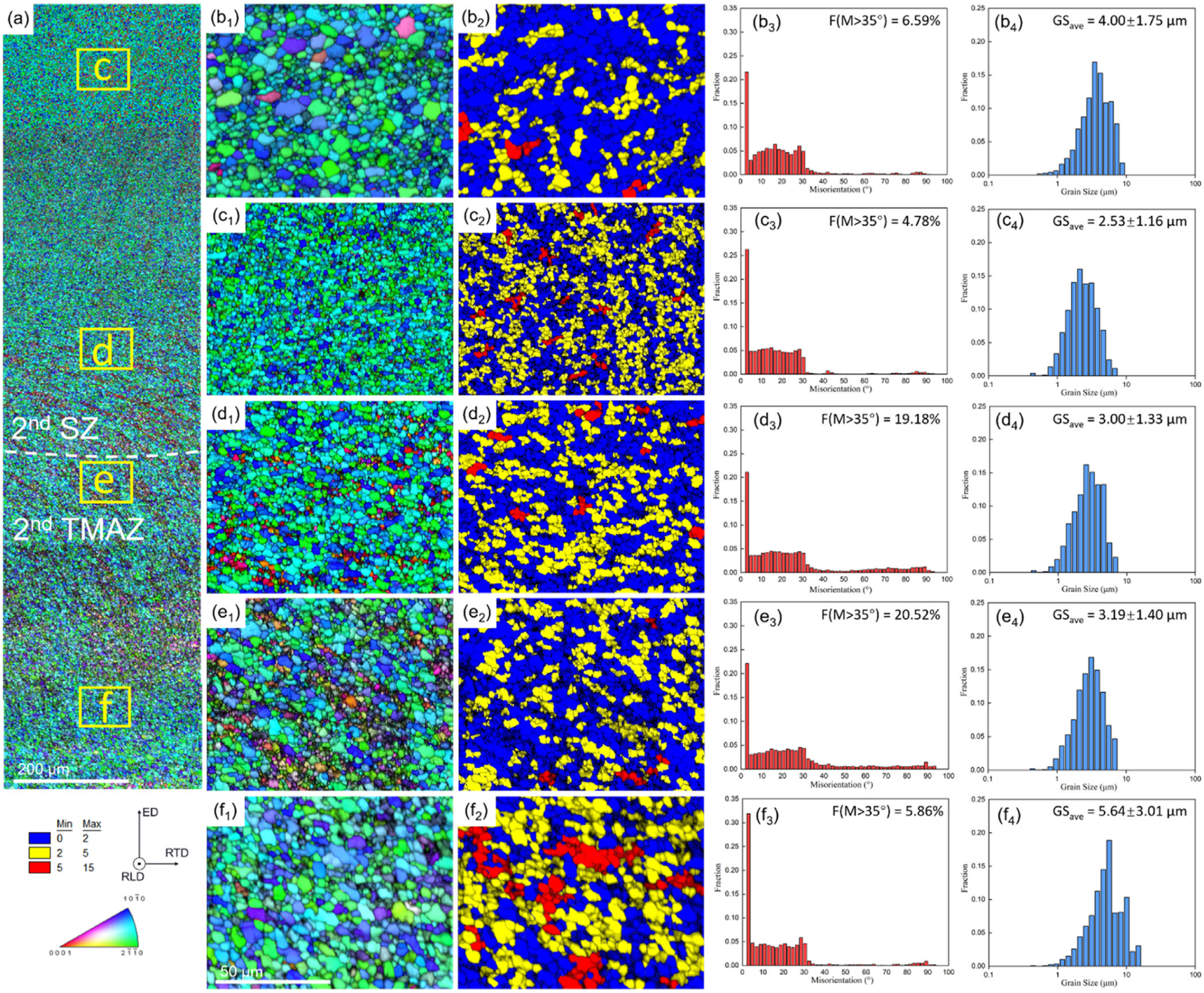

Fig. 10. (a) Microstructures of transition zone between SZ and TMAZ in MP-CFP marked as region a in Fig. 9(b_2) obtained via “stop-action” experiment. (b) Microstructure of SZ in the rod marked as region b in Fig. 9(b_2). (c–f) Microstructure corresponds to regions c–f inside the yellow rectangle in (a). (b_1–f_1) IPFs, (b_2–f_2) GOS maps, (b_3–f_3) misorientation distribution, (b_4–f_4) grain size distribution with average grain size.

basal texture. The microstructure evolutions during SP-CFP and MP-CFP are also different because of the change of microstructure before the final plunge stage. In SP-CFP, the main recrystallization mechanism is PSN and DTN due to the large grain size and secondary phase particles, while SBN and GBN play a main role attributed to grain refinement and texture strengthening in MP-CFP. Additionally, the reason for no further improvement of mechanical properties when more passes are adopted might be that the increase of processing passes cannot further change the grain size and texture before the final plunge stage.

4.2. Effects of microstructure on mechanical performance

The differences in material evolution between SP-CFP and MP-CFP result in changes to the microstructural characteristics, particularly the texture. Consequently, the MP-CFP rod exhibits a weaker basal texture in the middle and at the top compared to the SP-CFP rod. Results on texture observation have implied that modified texture by MP-CFP is the potential reason for the alleviation of local strain concentration at the top of the rod, and the improvement of mechanical performance. In this section, the compression deformation mechanism of the CFPed sample with gradient texture orientations was investigated to explain the phenomenon of an inhomogeneous strain field along the compression direction. Then the effects of texture intensity were analyzed to understand the improvement in mechanical performance after MP-CFP. Additionally, the effects of the edge part of the CFPed rod were further examined to verify the developed compression deformation mechanism.

4.2.1. Compression deformation mechanism

To elucidate the phenomenon of inhomogeneous strain field along compression direction during the compression test of the CFPed rod, as shown in Fig. 2, a detailed investigation into the compression deformation mechanism was undertaken for subsequent comprehension of the improvement in mechanical properties after MP-CFP by decreasing local strain concentration. After CFP, a special convex dome shape basal texture with gradient texture orientations was produced compared to the as-cast state with random orientation. The angle (φ) between the [0002] peak and ED direction increased with the radius of the CFPed rod, leading to notable differences in local mechanical behavior and properties. The Schmid Factor (SF), commonly used to assess the ease of slip ac-

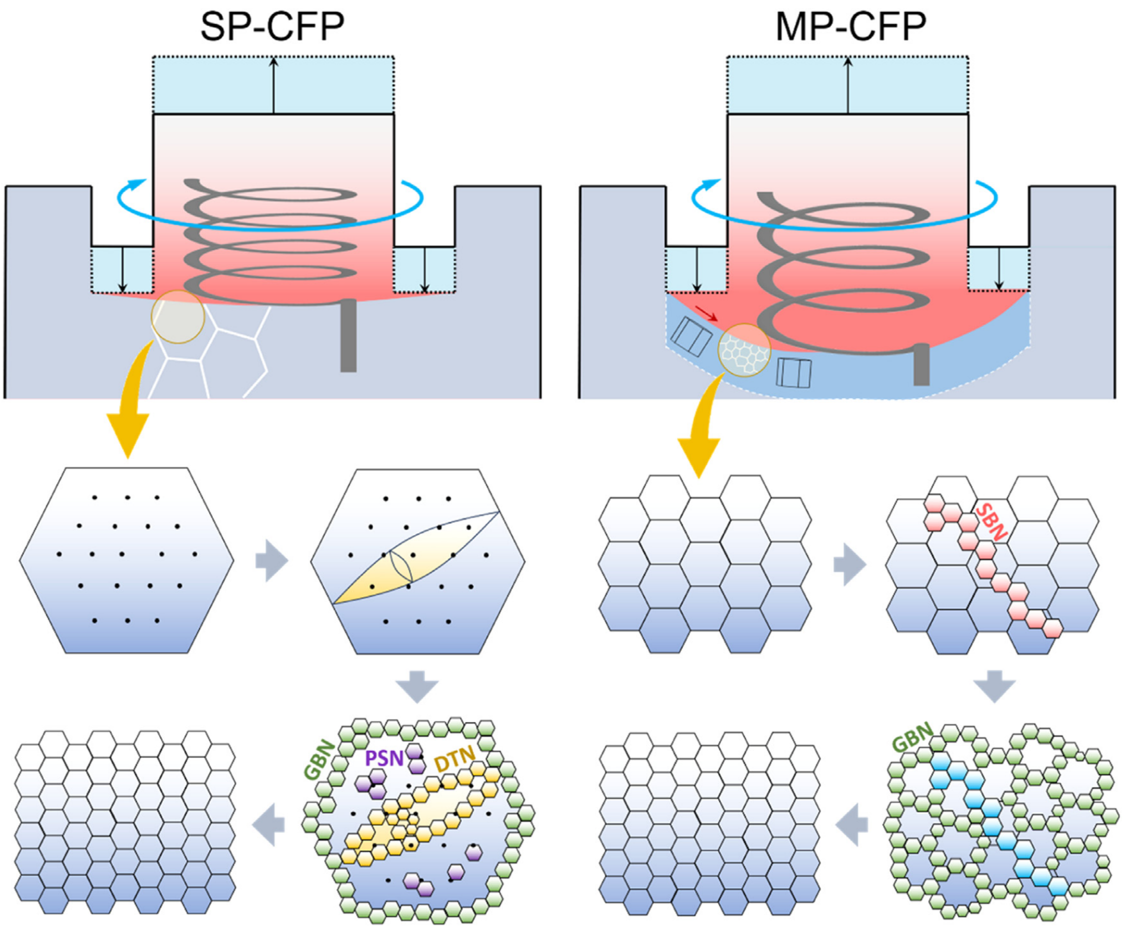

Fig. 11. Schematic material flow behavior and microstructure evolution during SP-CFP and the final plunge stage of MP-CFP. In SP-CFP, the large original grains with random texture lead to higher shear strain ahead of the SZ, presenting spiral distributed CNTs with low helix angle. After prior processing pass, grains are refined and texture strengthens, decreasing the shear strain ahead of the SZ. During SP-CFP, the main recrystallization mechanisms include the initial twinning of the original large grains, followed by DTN at the twinning boundaries, PSN at the secondary particles, and GBN at the grain boundaries. In the case of MP-CFP, SBN firstly starts due to strong basal texture, then the SBN grains rotate and GBN is the main recrystallization mechanism due to the refined grains.

tivation, closely related to yield strength [50,51], was employed in the analysis. The SF is calculated as follows:

$$\mathrm{SF} = \cos(\Phi)\cos\left(\lambda\right) \tag{1}$$

where Φ represents the angle between the stress and the normal direction of the slip/twinning plane, and λ is the angle between the direction of the load and the slip/twinning direction. It has been widely accepted that basal slip and tension twinning are much easier to activate than non-basal slip at room temperature due to their low CRSS, so basal slip and tension twinning play a very important role in terms of the mechanical properties of Mg alloys. Thus, the SF values for three basal <*a*> slip system variants, *i.e.* $(0001)[11\bar{2}0]$, $(0001)[2\bar{1}\bar{1}0]$ and $(0001)[1\bar{2}10]$, and six $\{10\bar{1}2\}$ extension twinning variants, *i.e.* $(10\bar{1}2)[10\bar{1}\bar{1}]$, $(01\bar{1}2)[01\bar{1}\bar{1}]$, $(\bar{1}102)[\bar{1}10\bar{1}]$, $(\bar{1}012)[\bar{1}01\bar{1}]$, $(0\bar{1}12)[0\bar{1}1\bar{1}]$ and $(1\bar{1}02)[1\bar{1}0\bar{1}]$, were calculated according to supplementary Table S4 under various φ angles, ranging from 0°–45°, and different rotation angles around the *c*-axis, ω, ranging from 0°–30°. Considering that the slip system is bidirectional and tension twinning is unidirectional, when the SF is negative, the SF of basal $\langle a\rangle$ slip is replaced by its absolute value, and the SF of tension twinning is set to 0. Maximum values of SF of basal slip and tension twinning are depicted in Fig. 12(a, b). As the φ angle increases, the SF of the basal slip increases, indicating that the basal slip is more likely to be activated at higher φ angles. However, the SF of tension twinning remains low, indicating that twinning is more challenging to activate when the φ angle is below 45°. The distribution of φ angles in regions 1 and 2 marked in Fig. 5(a), representing the center and the edge of the rod, respectively, were analyzed, as shown in Fig. 12(c), revealing that φ at the center peaked at approximately 10°, while it is significantly higher near the edge, reaching about 30°. Consequently, basal slip near the edge is more prone to activation, resulting in lower yield strength in this region. The distribution of SF in regions 1 and 2 was analyzed in Fig. 12(d), verifying that the SF near the edge was higher than that at the center.

To further analyze and understand the compression deformation mechanism of the CFPed rod with strong basal texture characterized by gradient orientation, the microstructure after compression at 3 % was characterized, as shown in Fig. 13. A large amount of convex arc traces has been formed after compression, as shown in Fig. 13(a). The microstructure in regions I and II marked in Fig. 13(a), representing the edge and center of the CFPed rod respectively, was further investigated by SEM with EBSD. By comparison between the IPF maps before and after the compression test, as shown in Fig. 13(b, c), no distinct difference in GBs and grain orientation is observed, meaning that twinning and grain nucleation are not activated during the compression test until 3 % strain. The morphology obtained by SEM and macro-SF distribution of basal slip with predicted basal slip traces in regions I and II were also analyzed, as shown in Fig. 13(d, e), respectively. In region I near the edge, most of the slip traces aligned to the basal slip plane, indicating that the basal slip is the main deforma-

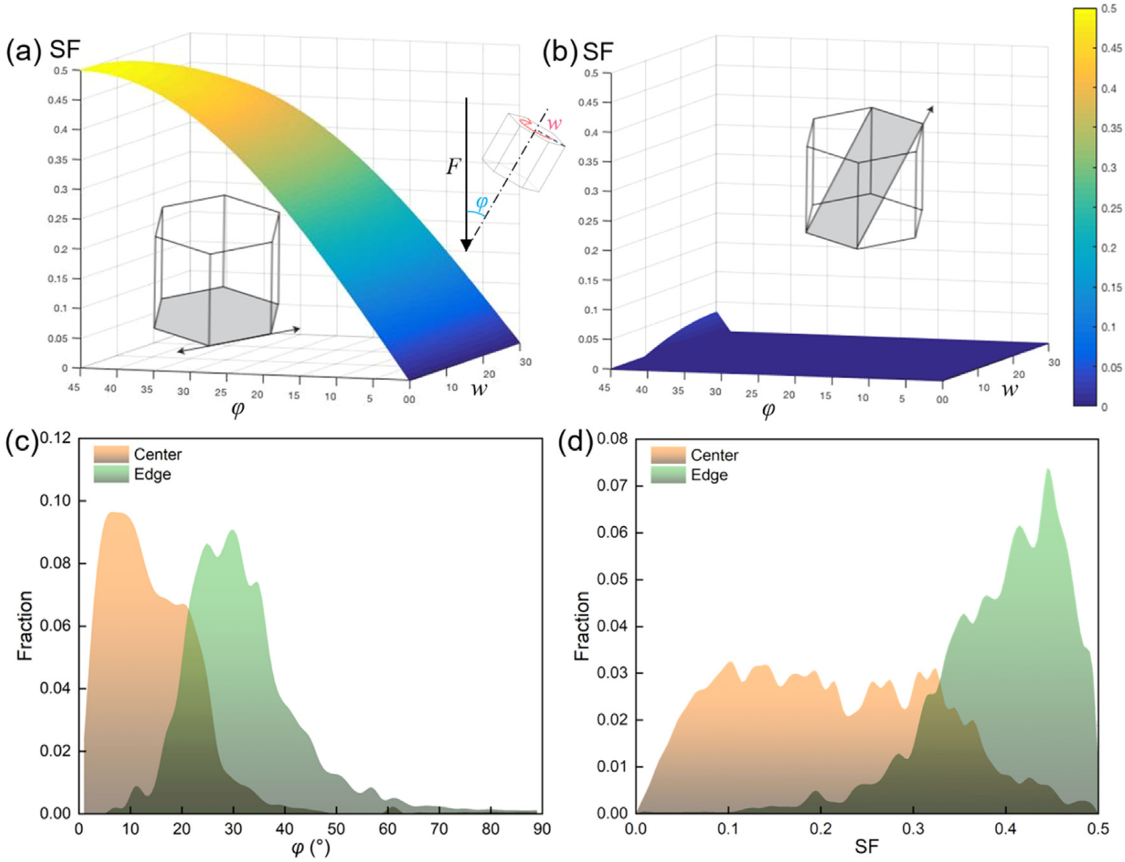

Fig. 12. Relationship between SF of (a) basal slip system and (b) tension twinning and φ, the angle between the c-axis of grains lattice and compression direction, and ω, rotation angle around c-axis. Distribution of (c) φ and (d) SF at the center and the edge of the CFPed rod, as shown in marked regions 1 and 2 in Fig. 5(a).

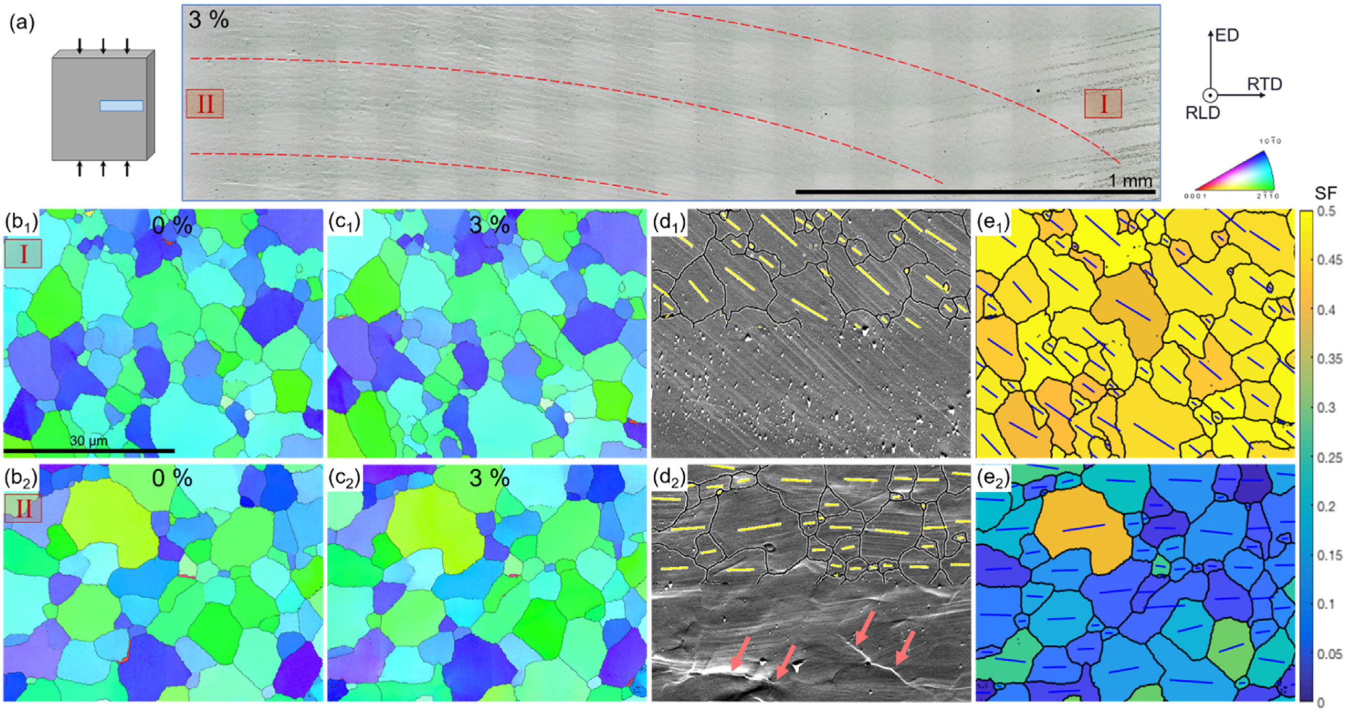

Fig. 13. Microstructure before and after plane compression test at a strain of 3 %. (a) Optical surface morphology after compression of 3 %. (b_1, b_2) IPF maps of initial local microstructure, (c_1, c_2) IPF maps after compression of 3 %. (d_1, d_2) corresponding surface morphology by SEM and (e_1, e_2) basal slip macro–SF distribution with predicted basal slip traces at regions I and II marked in (a).

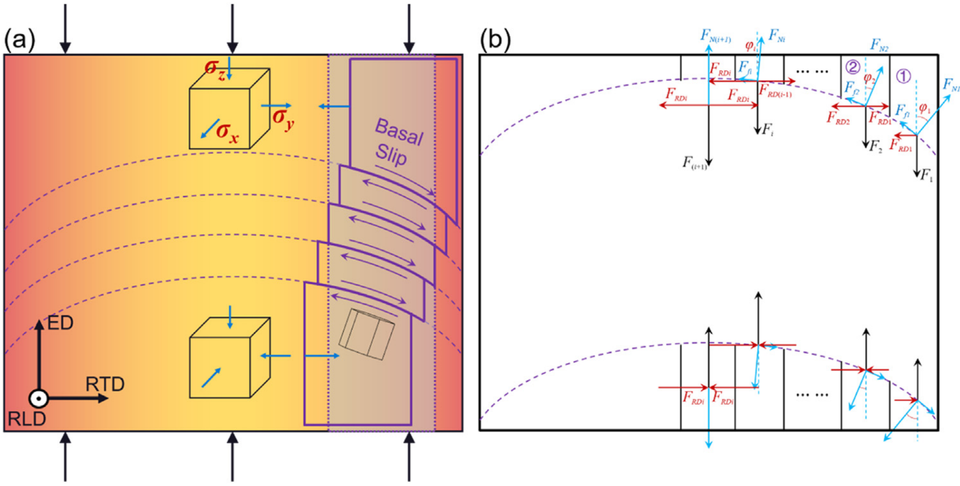

Fig. 14. (a) A schematic diagram illustrating the compression mechanism of a CFPed rod. (b) Force analysis based on a simple ideal model, in which different parts of the processed rod with different diameters are regarded as rigid bodies, while the only activated basal shear strain during the compression test is considered as a sliding interface.

tion mechanism. The basal slip SF of most grains exhibits a much higher value due to a higher φ angle, as shown in Fig. 13(e_1), and trace lines form an angle of approximately 45° with the horizontal plane. In region II at the center, except for basal slip traces inside grains, undulations at GBs, marked by red arrows in Fig. 13(d_2), are detected, indicating that the deformation at GBs also plays an important role during compression. The basal slip SF of most of the grains exhibits low value due to a low φ angle, as shown in Fig. 13(e_2), presenting a nearly horizontal basal slip tracer line. Since the activation of basal slip with slip planes nearly perpendicular to the compression direction cannot create enough compression deformation as those at the edge, deformation at GBs is activated at the center to match compression strain between the center and edge of the CFPed rod, leading to GBs undulations.

The special convex dome shaped basal texture with gradient orientation of the basal plane in CFPed rod, as shown in Fig. 14, leads to a global convex shear trace during compression deformation, as shown in Fig. 13(a). During the compression test, since the basal slip is easier to activate near the edge due to high SF values, as shown in Fig. 12, the material at the edge preferentially tends to plastically deform due to the tilted extremely strong basal texture. A simplified ideal model based on stress/force analysis was proposed to illustrate the compression deformation mechanism and explain the phenomenon of inhomogeneous strain field along compression direction, as shown in Fig. 14. In the model, the subregions of the processed rod are regarded as rigid bodies, while the interfaces of the subregions, where the basal shear strains are activated, are considered as the sliding interfaces. Fig. 14(a) illustrates the material deformation behavior of each interface. When the applied local compression stress exceeds the yield strength of the edge material, the edge with a strong basal texture tends to deform anisotropically. In this process, the material in the upper layer tends to deform outwards, while the material in the lower layer deforms inwards. According to the detailed force analysis, as shown in Fig. 14(b), Subregion 1, located at the edge of the upper layer, experiences the local compression force F_1. At the same time, basal plane sliding occurs between the upper and lower layers, generating the tangential inward resistance force, F_{f1}, and plane normal force, F_{N1}. To maintain mechanical balance, the horizontal tensile force from adjacent Subregion 2, F_{RD1}, develops, and its direction is inward. Likewise, F_{RDi} develops at each subregion of the upper layer. Conversely to the upper layer, the material of the lower layer tends to flow inward, as a result, compression stresses instead of tension stress develop at each subregion of the upper layer, as illustrated in Fig. 14(a). The equivalent of von Mises stress σ_{vm} is calculated by

$$\sigma_{vm} = \sqrt{[\left(\sigma_x - \sigma_y\right)^2 + \left(\sigma_y - \sigma_z\right)^2 + (\sigma_z - \sigma_x)^2]/2} \tag{2}$$

where σ_z is the compression stress along ED with a negative value, and the value of tensile σ_x at the upper layer is positive while that at the lower layer is negative. Thus, the von Mises stress at the upper layer is larger than that at the lower layer, providing an explanation for the observed higher local strain at the top of the CFPed rod when the compression stress exceeds the yield strength, as shown in Fig. 3.

4.2.2. Effects of texture intensity distribution on compression behaviors

As previously discussed, MP-CFP samples exhibit better compression properties compared to SP-CFP, with a more homogeneous strain distribution during compression deformation. Most of the microstructure characteristics except for texture are similar between SP-CFP and MP-CFP, indicating that texture plays an important role in the improvement of compression properties in MP-CFP. The I_{max} of local texture at the rotation axis and macrotexture at the upper and middle section of the rod obtained with MP-CFP are notably lower compared to SP-CFP, as shown in Figs. 6 and 7(a). It has been reported that weaker texture contributes to an enhancement in yield strength, as increased misorientation between neighboring grains impeded the transfer of slip systems across grains [52]. The geometrical compatibility factor (m'), describing strain transfer across a boundary has been usually used to evaluate the ease of transference of slip and/or twinning, as calculated as [53,54]:

$$m' = \cos(\alpha) \cos\left(\beta\right) \tag{3}$$

where α represents the angle between the normal direction of slip and/or twinning planes, and β is the angle between slip directions and/or twinning shear direction in two adjacent grains. Higher m' values indicate easier transference of slip and/or twinning across the boundary.

To investigate the effects of texture intensity on compression property, the m' maps of the basal slip system in all grain boundaries at the top of the rod obtained by SP-CFP and MP-CFP were calculated and illustrated in Fig. 15(a, b), respectively. The statistical distribution of the m' value of the basal slip system is presented in Fig. 15(c). In the case of SP-CFP, the m' values at the top of the rod are predominantly high, ranging from 0.7 to 1.0. On the other hand, a significant fraction of m' values at the top of the rod with

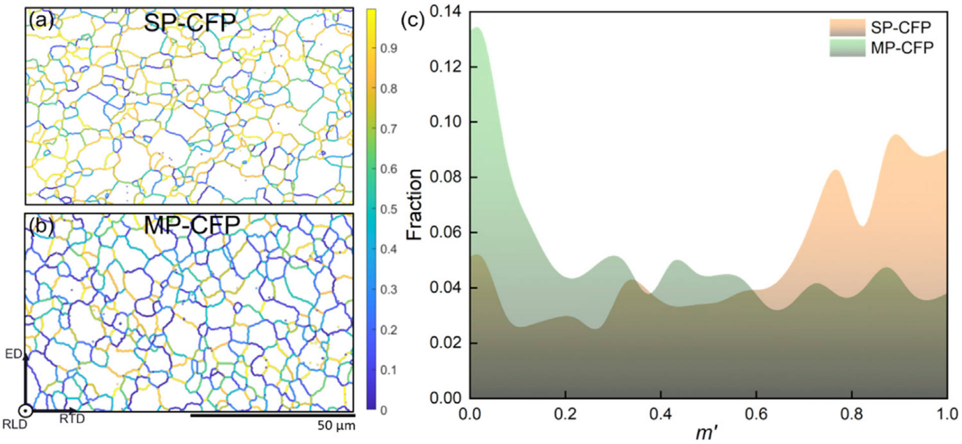

Fig. 15. The geometrical compatibility factor (*m*') of the basal slip system in all grain boundaries at the top of the rod produced by (a) SP-CFP and (b) MP-CFP. (c) The statistical distribution of *m*' value of basal slip system in (a, b).

MP-CFP is below 0.1, considerably lower than in SP-CFP. This signifies that the grain boundaries at the top of the rod with MP-CFP exhibit higher resistance to slip, inhibiting local strain concentration at the top compared to SP-CFP, as shown in Fig. 3, and contributing to the observed increase in yield strength, as shown in Fig. 2.

Upon surpassing the yield point during compression, strain concentration occurs primarily at the top of the rod with SP-CFP due to the introduction of horizontal tensile stress at the top, while the local strain at the middle and bottom remains at similarly low values. Conversely, the weakened texture at the top of the rod with MP-CFP enhances the local strength by inhibiting the slip transference, leading to lower strain concentration at the top, resulting in a gradually increasing gradient of local strain along the compression direction. This local strain gradient facilitates the introduction of triaxial compressive stresses at the bottom, as shown in Fig. 14, hindering the initiation and propagation of fracture cracks, and enhancing the ductility of the material at the bottom [55]. Consequently, the UCS and failure plastic strain of the rod with MP-CFP are higher, and the fracture position shifts from the bottom to the middle of the rod, as shown in Fig. 3(a).

4.2.3. Effects of the edge part of the processed rod on mechanical properties

As discussed above, the edge part of the processed rods exhibits high basal SF during compression tests due to its tilted basal pole peak, as shown in Fig. 12. This edge with a tilted basal pole peak is produced with a radius ranging about 2–3 mm due to friction from the plunging shoulder [21]. Additionally, the edge of CFPed rod with high SF of basal slip exhibits the easier activated basal slip system, leading to different horizontal stress applied on different layers and inhomogeneous strain field along the compression direction, according to the compression deformation mechanism analysis in Fig. 14. To understand the effects of the edge part on mechanical properties and verify the analysis of compression deformation mechanism of SP-CFP and MP-CFP samples, compression properties of CFPed samples with diameter of 5 mm, machined by removal of the edge part of processed rods were characterized and compared with the original rods with 6 mm diameter, as shown in Table 1 and Fig. S6. Smaller diameter samples (5 mm) exhibits higher CYS and UCS, since the edge with higher basal SF, *i.e.* lower yield strength, is partially removed. However, the failure plastic strain of samples with smaller diameters also decreases, indicating that the edge part helps to increase the plasticity of the processed rod. The existence of the edge part dispersed the distribution of the *c*-axis direction, which might be the main reason for the improvement in terms of plasticity. The effects of the gradient basal texture on plasticity will be further investigated in the future.

Table 1
Comparison of mechanical properties of SP-CFP and MP-CFP samples with different diameters.

Mechanical properties	Diameter (mm)	SP-CFP	MP-CFP	Improvement compared to SP-CFP rods (%)
CYS	6	175 MPa	205 MPa	17.1
	5	238 MPa	265 MPa	11.3
UCS	6	287 MPa	362 MPa	26.1
	5	349 MPa	391 MPa	12.0
Failure plastic strain	6	3.2 %	5.3 %	65.5
	5	2.4 %	3.3 %	37.5

Additionally, the strain field during the compression test of processed samples with diameter of 5 mm was determined by DIC, as shown in Fig. 16. The strain fields along gauge pattern in compression direction of samples obtained by SP-CFP and MP-CFP are more homogeneous compared with the original rods with 6 mm diameter, as shown in Fig. 3, indicating that the strain concentration and inhomogeneous strain field in compression direction are attributed to the effects of the edge part. This verifies the developed compression deformation mechanism in Fig. 14. The removal of the partial edge with high basal SF would alleviate anisotropy deformation at the edge. As a result, the tensile stress in RD applied on the upper layers of the rod decreases, leading to a more homogeneous strain field distribution along ED. MP-CFP could also further enhance CYS, UCS, and failure plastic strain of the processed rod with lower diameter by weakening the basal texture and homogenizing the strain field, as shown in Fig. 16(b), but the improvement in mechanical properties, especially UCS and failure plastic strain, diminishes with a reduction in the diameter of the rod. The removal of the partial edge part alleviates the local strain concentration at the top of the processed rod obtained by SP-CFP, weakening the effects of the intensity of texture at the upper part of the rod on mechanical properties.

In summary, the convex dome shaped basal texture produced by SP-CFP results in the edge part exhibiting high basal SF (Fig. 12). This edge part is more prone to yield due to the activation of basal slip in a similar direction (Fig. 13), leading to anisotropic deformation and introducing horizontal tensile stress in the upper layers of the CFPed rod (Fig. 14). This horizontal tensile stress causes strain concentration at the top of the rod during compression (Fig. 3). MP-CFP alleviates this strain concentration in the upper layer by weakening the basal texture and improving *m*' (Fig. 15), result-

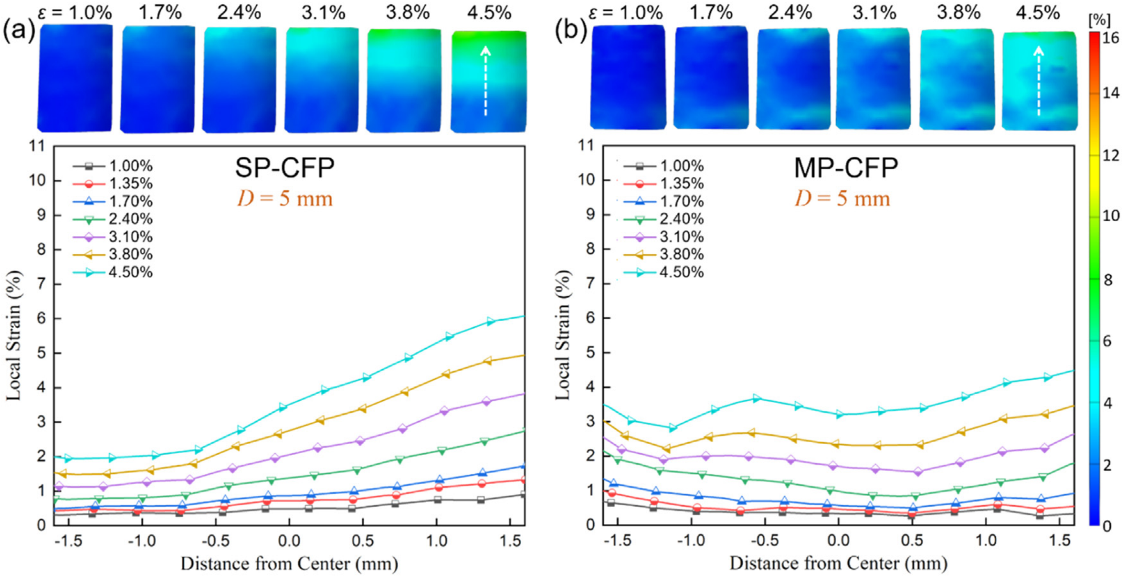

Fig. 16. Captured image series of equivalent strain field evolution as well as strain profile along gauge pattern in compression direction at different global strains of (a) SP-CFP and (b) MP-CFP samples with a diameter of 5 mm during compression test.

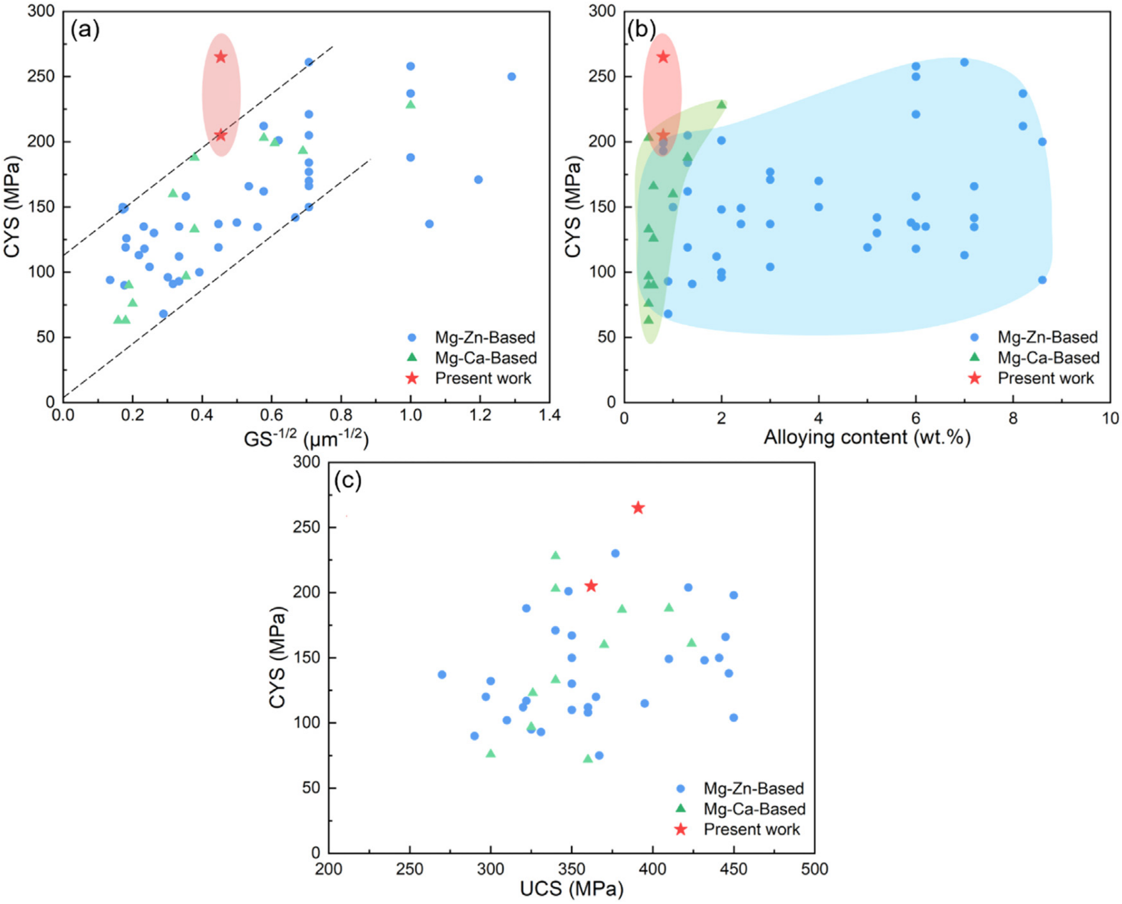

Fig. 17. Comparison of mechanical properties of MP-CFP ZX00 alloy to reported non-REE containing Mg-Zn [10,11,13,18,56–74] and Mg-Ca-based [75–77] alloys obtained by other SPD methods. (a) CYS and GS, (b) CYS and alloying contents of various Mg alloys. (c) CYS and UCS of various Mg alloys with low alloying content (< 5 wt.%).

ing in a more homogeneous and gradient strain field along the ED (Fig. 3), which enhances the mechanical properties. When the partial edge part is removed, the strain concentration in the upper layer is alleviated (Fig. 16), diminishing the improvement achieved by weakening the texture using MP-CFP. This verifies the developed compression deformation mechanism.

4.3. Advantages and prospects of CFP

CYS is an important value since the material should keep enough deformation resistance and safety when it is subjected to high stress in application as an implant material. CYS and GS of the MP-CFPed ZX00 alloy from the present study are compared to Mg-Zn and Mg-Ca-based alloys obtained by other SPD methods in the literature [10,11,13,18,56–77], as shown in Fig. 17(a). The relationship between CYS and GS of other Mg alloys presents a Hall-Patch relationship with a slope of about 200 MPa $\mu m^{-0.5}$, and the optimal strategy of mechanical properties by conventional processing method is mainly grain refinement. However, the Hall-Patch relationship does not apply to the material produced by CFP due to the special texture after processing. Even though the GS is not the smallest compared with other Mg alloys, the CYS of MP-CFP ZX00 alloy after texture modification showcases a competitive value compared to other Mg-Zn and Mg-Ca-based alloys attributed to the texture characteristics. Additionally, the CYS and alloying content of the MP-CFPed ZX00 alloys from the present study are compared to Mg-Zn and Mg-Ca-based alloys obtained by other SPD methods, as shown in Fig. 17(b). The MP-CFPed ZX00 alloys demonstrate high CYS despite containing fewer alloying elements, which typically enhances corrosion resistance and reduces costs [11,78]. CYS and UCS of various Mg alloys with low alloying content ($<$ 5 wt.%) were compared, as shown in Fig. 17(c). According to the design criteria for biodegradable bone-fixation implants proposed by Erinc et al. [79], the candidate materials should have a CYS greater than 182 MPa and a UCS exceeding 230 MPa. The MP-CFPed ZX00 alloy demonstrates competitive performance, meeting these requirements. Comprehensively considering the short processing time and high processing efficiency of the CFP method, and the mechanical properties of the products, CFP has great potential for future application.

Additionally, the failure strain of the CFPed rod improves as the fraction of the edge part with high basal SF increases, as shown in Table 1, while the strength remains high. This indicates that the convex dome shaped basal texture, which combines a center part with low basal SF and an edge part with gradually increasing basal SF, produced by CFP is a new potential strategy to achieve both high strength and ductility. The fraction of the edge part with high basal SF can be adjusted by changing the diameter of the processing tool or machining cut, and its effects on strength and ductility can be further investigated in the future.

5. Conclusions

In the present study, a MP-CFP was introduced to enhance the mechanical properties of ZX00 alloy by modifying its texture. A comprehensive examination of mechanical properties and microstructure was conducted, incorporating the use of the “stop action” technique and tracer experiments to analyze material flow behavior and microstructural evolution. Additionally, DIC during compression tests and calculations of SF and geometrical compatibility factor *m*’, were performed to elucidate the compression mechanism. The key findings are summarized as follows:

(1) Compared to SP-CFP, MP-CFP improves yield strength, ultimate strength, and failure strain significantly. Comparative analysis of SP-CFP reveals a remarkable increase of 11 %, 28 %, and 66 % in CYS, UCS, and failure plastic strain, respectively. Moreover, the CYS obtained by MP-CFP could reach a competitive value of approximately 265 MPa.

(2) The first pass of any MP-CFP effectively transforms the as-cast material, characterized by large grains ($>$ 1 mm) and random texture into fine grains (approximately 5–6 µm) with a strong basal texture. After the second plunge stage, the grain size does not change significantly. The recrystallization mechanism observed ahead of the stir zone near the root of the rod during the second plunge stage primarily involves shear band nucleation and grain boundary nucleation. Continuous dynamic recrystallization is noted in the rod under low shear strain, accompanied by an increase in misorientation and grain size.

(3) The microstructure after first pass processing, featuring fine grains and a strong basal texture, exhibits increased deformability and flow during the subsequent plunge stage of MP-CFP. This results in a low shear strain and complex material flow behavior. The orientation of grains near the rotation axis at the top and middle of the rod after MP-CFP proves to be inhomogeneous, resulting in a diminished intensity of local basal texture and macrotexture.

(4) The inhomogeneous distribution of local strain along the compression direction is attributed to the dome-shaped basal texture following CFP. Activation of basal slip at the edge of the rod with a high SF facilitated horizontal tensile stress at the top of the rod. The low intensity of basal texture, coupled with low *m*’ at the top of the rod after MP-CFP, effectively hindered slip transfer across grain boundaries. This contributes to the alleviation of local strain concentration at the top and a gradient strain field along the compression direction, ultimately leading to an improvement in mechanical properties.

Declaration of competing interest

The authors declare that they have no known competing financial interests or personal relationships that could have appeared to influence the work reported in this paper.

CRediT authorship contribution statement

Ting Chen: Writing – original draft, Visualization, Methodology, Investigation, Formal analysis, Conceptualization. **Banglong Fu:** Writing – review & editing, Validation, Methodology, Conceptualization. **Uceu F.H.R. Suhuddin:** Writing – review & editing, Resources. **Tong Shen:** Writing – review & editing, Investigation. **Gaohui Li:** Writing – review & editing, Methodology. **Emad Maawad:** Writing – review & editing, Investigation. **Junjun Shen:** Supervision, Conceptualization. **Jorge F dos Santos:** Supervision, Project administration. **Jean Pierre Bergmann:** Writing – review & editing, Supervision. **Benjamin Klusemann:** Writing – review & editing, Supervision, Funding acquisition.

Acknowledgments

Ting Chen thanks the China Scholarship Council for the Award of a Fellowship (No. 202006230137). Benjamin Klusemann acknowledges funding by the Deutsche Forschungsgemeinschaft (DFG, German Research Foundation) - project number 544306307. Banglong Fu acknowledge the financial support of the National Natural Science Foundation of China (Grant No. 52405386) and State Key Laboratory of Precision Welding & Joining of Materials and Structures (Grant No. MSWJ-24M13). The authors acknowledge DESY (Hamburg, Germany), a member of the Helmholtz Association HGF, for the provision of experimental facilities. Parts of this research were carried out at PETRA III P07 beamline, which is partly operated by Helmholtz-Zentrum Hereon. The authors are grateful to Mr. Günter Meister and Mr. Gert Wiese from Helmholtz-Zentrum Hereon, Institute of Metallic Biomaterials, for the provision of the base materials used in this study and the guidance of the metallographic preparation. The technical support of Mr. Menno Peters and Ms. Camila Caroline de Castro, from Helmholtz-Zentrum Hereon, Institute of Material and Process Design during this work is gratefully acknowledged.

Supplementary materials

Supplementary material associated with this article can be found, in the online version, at doi:10.1016/j.jmst.2025.01.026.

References

[1] Y. Zheng, X. Liu, D. Shen, W. Li, Y. Cheng, M. Yang, Y. Kou, B. Jiang, J. Mater. Sci. Technol. 147 (2023) 132–144.
[2] Y. Xin, T. Hu, P. Chu, Acta Biomater. 7 (2011) 1452–1459.
[3] J. Walker, S. Shadanbaz, T.B. Woodfield, M.P. Staiger, G.J. Dias, J. Biomed. Mater. Res. B 102 (2014) 1316–1331.
[4] B. Peng, H. Xu, F. Song, P. Wen, Y. Tian, Y. Zheng, J. Mater. Sci. Technol. 182 (2023) 79–110.
[5] Z. Pu, J.C. Outeiro, A.C. Batista, O.W. Dillon Jr, D.A. Puleo, I.S. Jawahir, Int. J. Mach. Tool. Manuf. 56 (2012) 17–27.
[6] S.S. Nene, B.P. Kashyap, N. Prabhu, Y. Estrin, T. Al-Samman, J. Alloys Compd. 615 (2014) 501–506.
[7] F. Cao, Z. Shi, G.-L. Song, M. Liu, M.S. Dargusch, A. Atrens, Corros. Sci. 90 (2015) 176–191.
[8] A. Incesu, A. Gungor, J. Mater. Sci. Mater. Med. 31 (2020) 1–12.
[9] A. Gungor, A. Incesu, J. Magnes. Alloys 9 (2021) 241–253.
[10] G. Wang, G. Huang, X. Chen, Q. Deng, A. Tang, B. Jiang, F. Pan, Mater. Sci. Eng. A 705 (2017) 46–54.
[11] P. Jiang, C. Blawert, R. Hou, J. Bohlen, N. Konchakova, M.L. Zheludkevich, Mater. Des. 185 (2020) 108285.
[12] J. Hofstetter, M. Becker, E. Martinelli, A. Weinberg, B. Mingler, H. Kilian, S. Pogatscher, P.J. Uggowitzer, J.F. Löffler, JOM 66 (2014) 566–572.
[13] J. Hofstetter, S. Rüedi, I. Baumgartner, H. Kilian, B. Mingler, E. Povoden-Karadeniz, S. Pogatscher, P.J. Uggowitzer, J.F. Löffler, Acta Mater. 98 (2015) 423–432.
[14] X. Wang, C. Chen, B. Miao, Z. Wang, H. Huang, S. Guan, G. Yuan, J. Mater. Sci. Technol. 183 (2024) 165–174.
[15] K. Edalati, A. Yamamoto, Z. Horita, T. Ishihara, Scr. Mater. 64 (2011) 880–883.
[16] C. Zhang, S. Zhu, L. Wang, R. Guo, G. Yue, S. Guan, Mater. Des. 96 (2016) 54–62.
[17] J. Horky, K. Bryła, M. Krystian, G. Mozdzen, B. Mingler, L. Sajti, Mater. Sci. Eng. A 826 (2021) 142002.
[18] E. Mostaed, M. Hashempour, A. Fabrizi, D. Dellasega, M. Bestetti, F. Bonollo, M. Vedani, J. Mech. Behav. Biomed. Mater. 37 (2014) 307–322.
[19] Y. Zhu, M. Zhou, Y. Geng, S. Zhang, T. Xin, G. Chen, Y. Zhou, X. Zhou, R. Wu, Q. Shi, J. Mater. Sci. Technol. 184 (2024) 245–255.
[20] W. Zhang, L. Tan, D. Ni, J. Chen, Y.-C. Zhao, L. Liu, C. Shuai, K. Yang, A. Atrens, M.-C. Zhao, J. Mater. Sci. Technol. 35 (2019) 777–783.
[21] T. Chen, B. Fu, J. Shen, U.F. Suhuddin, B. Wiese, Y. Huang, M. Wang, J.F. dos Santos, J.P. Bergmann, B. Klusemann, J. Magnes. Alloys 12 (2023) 516–529.
[22] C.C. de Castro, J. Shen, J.F. dos Santos, B. Klusemann, J. Mater. Process. Technol. 318 (2023) 118018.
[23] C.C. de Castro, A.M. Neves, B. Klusemann, J. Magnes. Alloys 12 (2024) 2298–2311.
[24] X. Li, L. Ren, Q. Le, L. Bao, P. Jin, P. Wang, C. Cheng, X. Zhou, C. Hu, J. Magnes. Alloys 9 (2021) 937–949.
[25] H. Zhang, H. Hao, G. Fu, B. Liu, R. Li, R. Wu, H. Pan, Acta Metall. Sin. (Engl. Lett.) 36 (2023) 335–342.
[26] C. Wang, A. Ma, J. Sun, H. Liu, H. Huang, Z. Yang, J. Jiang, J. Alloys Compd. 793 (2019) 259–270.
[27] F.R. Elsayed, N. Hort, M.A. Salgado Ordorica, K.U. Kainer, Mater. Sci. Forum 690 (2011) 65–68.
[28] C.D. Barrett, A. Imandoust, A.L. Oppedal, K. Inal, M.A. Tschopp, H. El Kadiri, Acta Mater. 128 (2017) 270–283.
[29] A. Hammersley, J. Appl. Crystallogr. 49 (2016) 646–652.
[30] S.-B. Yi, C.H.J. Davies, H.-G. Brokmeier, R. Bolmaro, K.U. Kainer, J. Homeyer, Acta Mater. 54 (2006) 549–562.
[31] B. Fu, J. Shen, U.F. Suhuddin, T. Chen, J.F. dos Santos, B. Klusemann, M. Rethmeier, Scr. Mater. 203 (2021) 114113.
[32] L. Tong, J. Chu, W. Sun, Z. Jiang, D. Zou, S. Liu, S. Kamado, M. Zheng, J. Magnes. Alloys 9 (2021) 1007–1018.
[33] S. Sandlöbes, S. Zaefferer, I. Schestakow, S. Yi, R. Gonzalez-Martinez, Acta Mater. 59 (2011) 429–439.
[34] P. Prangnell, C. Heason, Acta Mater. 53 (2005) 3179–3192.
[35] W. Hutchinson, M. Barnett, Scr. Mater. 63 (2010) 737–740.
[36] J. Wang, Y. Chen, Z. Chen, J. Llorca, X. Zeng, Acta Mater. 217 (2021) 117151.
[37] S. Zhou, C. Deng, S. Liu, Y. Liu, J. Zhu, X. Yuan, Mater. Charact. 184 (2022) 111686.
[38] Z. Li, G. Wu, J. Yu, J. Wang, J. Han, H. Cui, Z. Zhang, J. Magnes. Alloys 11 (2023) 2558–2584.
[39] O. Sitdikov, R. Kaibyshev, Mater. Trans. 42 (2001) 1928–1937.
[40] K. Zhang, Z. Shao, J. Jiang, Mater. Des. 194 (2020) 108936.
[41] D. Guan, W.M. Rainforth, L. Ma, B. Wynne, J. Gao, Acta Mater. 126 (2017) 132–144.
[42] D. Guan, W.M. Rainforth, J. Gao, L. Ma, B. Wynne, Acta Mater. 145 (2018) 399–412.
[43] I. Basu, T. Al-Samman, G. Gottstein, Mater. Sci. Eng. A 579 (2013) 50–56.
[44] P. Peng, K. Zhang, J. She, A. Tang, J. Zhang, K. Song, Q. Yang, F. Pan, J. Alloys Compd. 861 (2021) 157958.
[45] J.D. Robson, D. Henry, B. Davis, Acta Mater. 57 (2009) 2739–2747.
[46] H. Fan, S. Aubry, A. Arsenlis, J.A. El-Awady, Scr. Mater. 112 (2016) 50–53.
[47] A. Jain, O. Duygulu, D. Brown, C. Tomé, S. Agnew, Mater. Sci. Eng. A. 486 (2008) 545–555.
[48] F. Han, X. Luo, K. Marthinsen, G. Wu, Z. Hou, X. Huang, J. Mater. Sci. Technol. 188 (2024) 169–182.
[49] S. Mironov, T. Onuma, Y. Sato, H. Kokawa, Acta Mater. 100 (2015) 301–312.
[50] S.R. Agnew, Ö. Duygulu, Int. J. Plast. 21 (2005) 1161–1193.
[51] W. Kim, S. Hong, Y. Kim, S. Min, H. Jeong, J. Lee, Acta Mater. 51 (2003) 3293–3307.
[52] J. Xu, B. Guan, Y. Xin, X. Wei, G. Huang, C. Liu, Q. Liu, J. Mater. Sci. Technol. 99 (2022) 251–259.
[53] Z.-Z. Shi, Y. Zhang, F. Wagner, P.-A. Juan, S. Berbenni, L. Capolungo, J.-S. Lecomte, T. Richeton, Acta Mater. 83 (2015) 17–28.
[54] H. Yu, Y. Xin, M. Wang, Q. Liu, J. Mater. Sci. Technol. 34 (2018) 248–256.
[55] X. Gao, T. Zhang, M. Hayden, C. Roe, Int. J. Plast. 25 (2009) 2366–2382.
[56] Y. Xiong, Q. Yu, Y. Jiang, Mater. Sci. Eng. A 710 (2018) 206–213.
[57] S. Lv, F. Meng, X. Lu, Q. Yang, X. Qiu, Q. Duan, J. Meng, J. Alloys Compd. 806 (2019) 1166–1179.
[58] J. She, P. Peng, L. Xiao, A. Tang, Y. Wang, F. Pan, Mater. Sci. Eng. A 765 (2019) 138203.
[59] S. Safi-Naqvi, W. Hutchinson, M. Barnett, Mater. Sci. Technol. 24 (2008) 1283–1292.
[60] L. Tong, M. Zheng, S. Kamado, D. Zhang, J. Meng, L. Cheng, H. Zhang, J. Magnes. Alloys 3 (2015) 302–308.
[61] S. Xu, K. Oh-Ishi, H. Sunohara, S. Kamado, Mater. Sci. Eng. A 558 (2012) 356–365.
[62] T. Homma, C. Mendis, K. Hono, S. Kamado, Mater. Sci. Eng. A 527 (2010) 2356–2362.
[63] S. Kamrani, C. Fleck, Mater. Sci. Eng. A 618 (2014) 238–243.
[64] L. Mackenzie, B. Davis, F. Humphreys, G. Lorimer, Mater. Sci. Technol. 23 (2007) 1173–1180.
[65] M. Jiang, C. Xu, T. Nakata, H. Yan, R. Chen, S. Kamado, J. Alloys Compd. 668 (2016) 13–21.
[66] A. Malik, Y. Wang, F. Nazeer, M.A. Khan, M. Sajid, S. Jamal, W. Mingjun, J. Alloys Compd. 858 (2021) 157740.
[67] C. Cui, W. Zhang, W. Chen, J. He, X. Chen, J. Hou, J. Magnes. Alloys 10 (2022) 2745–2760.
[68] R. Liu, J. Wang, L. Wang, X. Zeng, Z. Jin, Metals 12 (2022) 693.
[69] J. Wang, G. Zhu, L. Wang, E. Vasilev, J.-S. Park, G. Sha, X. Zeng, M. Knezevic, J. Mater. Sci. Technol. 84 (2021) 27–42.
[70] M. Hradilová, D. Vojtěch, J. Kubásek, J. Čapek, M. Vlach, Mater. Sci. Eng. A 586 (2013) 284–291.
[71] E. Mostaed, A. Fabrizi, D. Dellasega, F. Bonollo, M. Vedani, J. Alloys Compd. 638 (2015) 267–276.
[72] M. Kavyani, G. Ebrahimi, H. Ezatpour, M. Jahazi, J. Magnes. Alloys 10 (2022) 1640–1662.
[73] P. Doležal, J. Zapletal, S. Fintová, Z. Trojanová, M. Greger, P. Roupcová, T. Podrábský, Materials 9 (2016) 880.
[74] J. Stráská, P. Minárik, S. Šašek, J. Veselý, J. Bohlen, R. Král, J. Kubásek, Metals 10 (2019) 35.
[75] K. Illkova, P. Dobroň, F. Chmelík, K. Kainer, J. Balík, S. Yi, D. Letzig, J. Bohlen, J. Alloys Compd. 617 (2014) 253–264.
[76] T. Wang, L. Jiang, R.K. Mishra, J.J. Jonas, Metall. Mater. Trans. A 45 (2014) 4698–4709.
[77] N.Y. Yurchenko, N. Stepanov, G. Salishchev, V. Serebryany, N. Martynenko, E. Lukyanova, L. Rokhlin, N. Birbilis, S. Dobatkin, Y. Estrin, J. Magnes. Alloys 10 (2022) 266–280.
[78] T. Akhmetshina, L. Berger, I. Basu, S. Montibeller, W. Rubin, A.M. Rich, R.E. Schäublin, J.F. Löffler, Acta Mater. 278 (2024) 120247.
[79] M. Erinc, W. Sillekens, R. Mannens, R. Werkhoven, Magnesium Technology, Springer, Berlin, Heidelberg, Germany, 2009.